



#### **PAPER**

# Self-similar blow-up solutions in the generalised Korteweg-de Vries equation: spectral analysis, normal form and asymptotics

To cite this article: S Jon Chapman et al 2024 Nonlinearity 37 095034

View the <u>article online</u> for updates and enhancements.

# You may also like

- Qualitative properties for solutions to subcritical fourth order systems
   João Henrique Andrade and João Marcos Do Ó
- <u>Transition of blow-up mechanisms in k-equivariant harmonic map heat flow</u>
  Pawe Biernat and Yukihiro Seki
- Concentrating solutions for a Liouville type equation with variable intensities in 2Dturbulence

Angela Pistoia and Tonia Ricciardi

# Self-similar blow-up solutions in the generalised Korteweg-de Vries equation: spectral analysis, normal form and asymptotics

S Jon Chapman<sup>1</sup>, M Kavousanakis<sup>2</sup>, E G Charalampidis<sup>3,4,\*</sup>, I G Kevrekidis<sup>5,6</sup> and P G Kevrekidis<sup>7</sup>

- <sup>1</sup> Mathematical Institute, University of Oxford, AWB, ROQ, Woodstock Road, Oxford OX2 6GG, United Kingdom
- <sup>2</sup> School of Chemical Engineering, National Technical University of Athens, Athens 15780, Greece
- Mathematics Department, California Polytechnic State University, San Luis Obispo, CA 93407-0403, United States of America
- <sup>4</sup> Department of Mathematics and Statistics, San Diego State University, San Diego, CA 92182-7720, United States of America
- Department of Chemical and Biomolecular Engineering, Johns Hopkins University, Baltimore, MD 21218, United States of America
- <sup>6</sup> Department of Applied Mathematics and Statistics, Johns Hopkins University, Baltimore, MD 21218, United States of America
- Department of Mathematics and Statistics, University of Massachusetts, Amherst, MA 1003-4515, United States of America

E-mail: echaralampidis@sdsu.edu

Received 27 October 2023; revised 15 May 2024 Accepted for publication 10 June 2024 Published 14 August 2024

Recommended by Dr Christian Klein



# **Abstract**

In the present work we revisit the problem of the generalised Korteweg–de Vries equation parametrically, as a function of the relevant nonlinearity exponent, to examine the emergence of blow-up solutions, as traveling waveforms lose their stability past a critical point of the relevant parameter p, here at p=5. We provide a *normal form* of the associated collapse dynamics, and illustrate how this captures the collapsing branch bifurcating from the unstable traveling branch. We also systematically characterise the linearisation spectrum of not only the traveling states, but importantly of the emergent collapsing waveforms

<sup>\*</sup> Author to whom any correspondence should be addressed.

in the so-called co-exploding frame where these waveforms are identified as stationary states. This spectrum, in addition to two positive real eigenvalues which are shown to be associated with the symmetries of translation and scaling invariance of the original (non-exploding) frame features complex patterns of negative eigenvalues that we also fully characterise. We show that the phenomenology of the latter is significantly affected by the boundary conditions and is far more complicated than in the corresponding symmetric Laplacian case of the nonlinear Schrödinger problem that has recently been explored. In addition, we explore the dynamics of the unstable solitary waves for p > 5 in the co-exploding frame.

Keywords: spectral analysis, self-similar blowup, normal form

Mathematics Subject Classification numbers: 35B06, 35B32, 35B44, 35C06, 34E10, 34E20, 47A75, 37G05, 37L10

#### 1. Introduction

This study centres around the investigation of the spectral stability of solutions to the generalised Korteweg–de Vries equation, denoted as gKdV hereafter:

$$\frac{\partial u}{\partial t} = -\frac{\partial^3 u}{\partial x^3} - \frac{\partial u^p}{\partial x},\tag{1}$$

where the nonlinearity exponent,  $p \ge 2$ , governs the behaviour of solutions that exhibit self-similar blow-up in finite time. The gKdV equation is a prototypical dispersive nonlinear partial differential equation (PDE) which possesses solitary waveforms due to the interplay of dispersion and nonlinearity [1, 2]. In addition to its central relevance to the description of water waves [3, 4], it also emerges through the continuum limit approximation [5] of the well-known Fermi–Pasta–Ulam–Tsingou (FPUT) lattice model [6, 7] in which p specifies the nonlinear exponent governing the FPUT's force law [8]. Specifically, for p = 2 and p = 3 the gKdV corresponds to the classical KdV [9] and the modified KdV (mKdV) models, respectively. Both KdV and mKdV are integrable [1, 10, 11] in the sense that they have an infinite number of conserved quantities and can be described as compatibility conditions of suitable Lax pairs [1, 3, 4]. The practical applications of KdV and mKdV span a broad range of fields, including shallow water dynamics, optical fibres, plasma physics, ion-acoustic solitons, and electric circuits, among others [2–4, 12–14].

While the KdV and mKdV equations are integrable, the gKdV equation for other values of the nonlinearity exponent, p, lacks integrability, to the best of our current understanding. However, when considering smooth functions that decay suitably fast as  $|x| \to \infty$ , the gKdV possesses three fundamental conserved quantities:

$$E_1 := ||u||_1 = \int_{-\infty}^{\infty} u \, \mathrm{d}x,$$
 (2a)

$$E_2 := \|u\|_2^2 = \int_{-\infty}^{\infty} u^2 \, \mathrm{d}x,\tag{2b}$$

$$E_3 := \frac{1}{2} \int_{-\infty}^{\infty} \left[ u_x^2 - \frac{1}{p+1} u^{p+1} \right] dx.$$
 (2c)

These quantities correspond to the conservation of mass, momentum and energy, respectively [15, 16]. The invariance of the gKdV equation under space and time translations is responsible, through Noether theory [17], for the second and third among these conservation laws, while the fundamental form of the gKdV as a conservation law leads to the conservation of mass. However, in addition to these key conserved quantities, the model also possesses a scale invariance:

$$u(x,t) \mapsto \lambda^{\frac{2}{p-1}} u(\lambda x, \lambda^3 t), \quad \lambda \neq 0.$$
 (3)

It is important to highlight that this transformation preserves the momentum in the critical case of p = 5 that will be further discussed below. This transformation group also leads to the notable fact that if u(x,t) is a valid solution, then u(-x,-t) is also a solution.

Even though the gKdV equation is not known to be integrable for most values of the non-linearity exponent, p (with the notable exceptions of p = 2 and p = 3), it admits traveling wave (TW) solutions parametrically as a function of p. These TW solutions are characterised by the following analytically available expression:

$$u(x,t) := Q(\xi) = \left(\frac{c(p+1)}{2}\right)^{\frac{1}{p-1}} \operatorname{sech}^{\frac{2}{p-1}} \left(\frac{\sqrt{c(p-1)}}{2}\xi\right),\tag{4}$$

where  $\xi := x - ct$ , and c denotes the wave speed. In [15], it was shown that the TW solution of equation (4) with c = 1 is linearly unstable for  $p \ge 5$ . Furthermore, it becomes evident that blow-up in finite time is possible when p > 5, corresponding to the super-critical case [18]. If p = 5, i.e. the critical case, solutions u to the gKdV exhibit global existence and temporal boundedness, granted that the initial data  $u_0$  satisfy the condition  $\|u_0\|_2 < \|Q\|_2$  [19]. This criterion is based on a Gagliardo-Nirenberg inequality argument [20]. Based on the same argument, it can be shown that solutions also globally exist and remain bounded for the subcritical case, p < 5. It is relevant to mention here also the work of [21] which showcased the exponential instability of the solitary wave for p > 5 through the presence of a real eigenvalue pair in the spectrum (leading to exponential growth), as a result of the change of monotonicity of the momentum  $E_2$  of the solution as a function of its speed.

Numerous efforts have been dedicated to numerically investigating blow-up solutions within the context of the gKdV equation; we briefly mention a few here. In the work of [22], a comprehensive approach to studying the instability of solitary waves leading to blow-up in a similarity form was introduced. This involved employing high-order numerical schemes in both spatial and time dimensions, supplemented with mesh adaptivity. The study centred on tracking the growth rate of various  $L^s$ -norms of the solution. The numerical computations carried out in [23] delved deeper into this phenomenon, and discovered how self-similar blow-up takes place for rapidly decaying solutions at  $|x| \to \infty$ . Notably, [23] argued that this blow-up phenomenon is intricately linked to the instability of TWs, and that the self-similar solutions inherit the stability that the TW solutions have relinquished. In parallel with the computation of self-similar profiles in [23], the work presented in [24] approached the self-similar blow-up problem within the gKdV framework as a bifurcation problem, and constructed an approximate invariant manifold that encompasses both TW and self-similar blow-up solutions. In [25], a numerical study of the stability of TWs was carried out by performing direct numerical simulations using exponential time differencing methods [26]. This was also the first study that performed computations of the fully dynamically rescaled form of the PDE. A significant finding in [25] was that TWs are unstable against being radiated away and blowing-up, thus numerically identifying the blow-up mechanism discussed in detail in [27, 28]. However, additional intriguing features were also identified such as the emergence of a dispersive shock wave (prior to collapse) in the small dispersion regime.

More recently, the research presented in [16] has delved into the supercritical regime, p > 5, resolving the structure of self-similar blow-up solutions, upon computing these solutions systematically as stationary ones. Their work involved the implementation of a dynamic rescaling technique using collocation and finite difference methods [29], and was complemented by a detailed analysis of the solutions' asymptotics (in space). Indeed, and alongside the sech-like shape of the self-similar profile in its core, the authors found that the solution features a slow algebraic decay to the left of the peak and a rapid (exponentially dominated) decay to the right [16]. It is important to highlight here the theoretical work of [30] that used modulation theory in order to derive leading-order dynamics close to collapse for the centre evolution of the collapsing solution (upon factoring out the relevant translation), its width evolution and the rescaled time dynamics of the rate of collapse (blow-up rate). For the centre, it is found that residual motion vanishes, the shrinkage rate of the solution width matches that of the amplitude growth. Finally, the rate of blow-up follows its own leading-order dynamics which is bounded by higher order terms. These results relate to the normal form dynamics identified in section 3.4 below; we discuss them further there.

In the present paper, we expand upon the above works, and not only focus on the construction of self-similar blow-up solutions within the gKdV framework, but also study their spectral stability, as well as obtain the normal form associated with the bifurcation that the TW solution (4) undergoes at the critical point of p = 5, in order to elucidate the onset of collapse. More specifically, we continue the long-term program of systematically characterizing the emergence of self-similarly collapsing waveforms as a bifurcation problem through the instability of regular solitary waveforms. This was initiated in the work of [31], which built on the earlier seminal works of [32–34] for the widely considered case of the nonlinear Schrödinger (NLS) model. The bifurcation structure of the problem was computed numerically and the spectral analysis of the emergent collapsing solutions in the self-similar frame was given. This was subsequently further elucidated in the work of [35] which obtained systematically, leveraging asymptotics beyond all orders, the normal form dynamics of the NLS model near the bifurcation point giving rise to the emergence of self-similarly collapsing waveforms. Lastly, in the context of NLS, our recent work of [36] led to a detailed understanding of both the point and the continuous spectrum of the stationary states in the self-similar frame, attributing the putative instabilities therein to the breaking (within this co-exploding frame) of original symmetries of translational and scaling invariance (see, also [37]).

Here, we accomplish both of the following goals for the gKdV model. We extract the associated normal form and showcase its pitchfork-like structure similarly to NLS, although we illustrate that, differently from the NLS case, exponentially small terms do not arise in the present gKdV setting. In the normal form identified, linear terms—emerging with an absolute value— and quadratic ones (in the blow-up rate G) are found to dominate the right hand side and the associated phenomenology near the bifurcation point. The symmetry of the normal form reflects the existence of solutions with both G and  $-G \neq 0$  (i.e. the 'pitchfork-like' feature of the normal form), yet the linear and quadratic terms are also reminiscent of a transcritical normal form.

At the same time, we provide a detailed analysis of the linearisation spectrum not only around the simpler solitonic waveforms, but also around the self-similarly collapsing states emerging past the critical bifurcation point of p=5. The latter states are found to feature a particularly complicated spectrum (especially as concerns the continuous spectrum), driven by the third derivative operator of the gKdV problem and the associated boundary conditions that we use for the collapsing waveforms. That turns out to be fundamentally different once

again from the simpler case of the NLS problem, although the two cases share the same type of apparent (yet dynamically innocuous) instabilities, stemming from the invariance with respect to translation and the invariance with respect to scaling of the original frame (as viewed in the co-exploding frame where the collapsing solution is stationary).

Our presentation is structured as follows. In the next section, we provide the overarching scaling formulation, connecting the TWs of the original frame and the self-similar solutions upon dynamic rescaling. We set up the associated stationary problems and boundary conditions thereof, and also illustrate how to formulate the corresponding linearisation problem. Then, the core of our findings is presented in section 3, which starts with the simpler (and well-known) spectral analysis of the traveling waveforms, and then proceeds to extend considerations to the self-similar structures. Both the point and the continuous spectrum of the latter is examined and, subsequently, the normal form of the associated collapse dynamics is elucidated. Finally, in section 4, we summarise our findings and present our conclusions, as well as a number of directions for further study.

# 2. Mathematical setup

We now set the stage for our forthcoming discussions within this work. Our approach follows the dynamic renormalisation technique described in [36] (and references therein). This approach allows us to rewrite the problem in the co-exploding frame through the ansatz:

$$u(x,t) := A(\tau)w(\xi,\tau), \quad \xi := \frac{x}{B(\tau)} + K(\tau), \quad \tau := \tau(t). \tag{5}$$

Here, A and B represent the solution's amplitude and width, and alongside the function K, all depend on the renormalised time,  $\tau$ . Upon inserting equation (5) into equation (1) and employing the chain rule, we arrive at:

$$\left(\frac{1}{A}\frac{\partial A}{\partial \tau}w + (K - \xi)\frac{1}{A}\frac{\partial A}{\partial \tau}\frac{\partial w}{\partial \xi} + \frac{\partial K}{\partial \tau}\frac{\partial w}{\partial \xi} + \frac{\partial w}{\partial \tau}\right)\frac{\partial \tau}{\partial t} = -\frac{1}{B^3}\left(\frac{\partial^3 w}{\partial \xi^3} + A^{p-1}B^2\frac{\partial w^p}{\partial \xi}\right)$$
(6)

after dividing both sides by A (where  $A \neq 0$ ). We balance the terms on the right-hand-side (RHS) of equation (6) by imposing the condition,  $A^{p-1}B^2 = 1$ , or equivalently:

$$A = B^{-2/(p-1)}, (7)$$

which leads to:

$$\frac{1}{A}\frac{\partial A}{\partial \tau} = -\frac{2}{p-1}\frac{1}{B}\frac{\partial B}{\partial \tau} = -\frac{2G}{p-1}, \quad G = G(\tau) := \frac{1}{B}\frac{\partial B}{\partial \tau}, \tag{8}$$

where G represents the rate of change of the solution's width, B. Additionally, if we demand time independence of the effective dynamics in the renormalised frame, it is relevant to use:

$$\frac{\partial \tau}{\partial t} = \frac{1}{B^3}.\tag{9}$$

Then, equation (6) simplifies to the renormalised gKdV equation:

$$\frac{\partial w}{\partial \tau} = -\frac{\partial^3 w}{\partial \xi^3} - \frac{\partial w^p}{\partial \xi} + G\left(\frac{2w}{p-1} + \xi \frac{\partial w}{\partial \xi}\right) - \left(KG + \frac{\partial K}{\partial \tau}\right) \frac{\partial w}{\partial \xi}.$$
 (10)

To reduce the dynamics to the case of a TW with speed c = 1, we require:

$$KG + \frac{\partial K}{\partial \tau} = -1. \tag{11}$$

Notice that this is in line with the formulation of [24] (see equation (6) therein). Importantly, and in order to unify the relevant formulations in different recent works, we remind the reader that the transformation discussed therein (in particular, using  $W(y) = G^{-2/(3p)}w(G^{-1/3}y - G^{-1})$ ) provides a matching of the problem considered with the setup of [16].

Consequently, equation (10) transforms, according to equation (11), into:

$$\frac{\partial w}{\partial \tau} = -\frac{\partial^3 w}{\partial \xi^3} - \frac{\partial w^p}{\partial \xi} + G\left(\frac{2w}{p-1} + \xi \frac{\partial w}{\partial \xi}\right) + \frac{\partial w}{\partial \xi}.$$
 (12)

As per the definition of G in equation (8), and the monotonic growth of  $\tau$  from equation (9), the solution's width, B, diminishes, signifying a contraction in its spatial extent—effectively,  $B_{\tau} < 0$ . Accordingly, self-similar blow-up solutions in *forward time* with respect to equation (1) correspond to steady-state solutions of equation (12) characterised by G < 0. To elaborate, as  $t \to t^*$  with  $t^* > 0$  representing the blow-up time in the original frame, then  $\tau \to \infty$  resulting in  $w(\xi,\tau)\mapsto w(\xi)$ , i.e., reaching a stationary self-similar profile for which  $G(\tau)\to \mathrm{const.}(<0)$ . Furthermore, the transformation  $\tau\mapsto -\tau$ ,  $G\mapsto -G$ , and  $\xi\mapsto -\xi$  leaves equation (12) invariant thereby permitting the existence of a self-similar solution that blows up in *backward time*. In other words, this solution appears to be 'coming back from infinity' characterised by  $G\to \mathrm{const.}(>0)$ . [The latter will be important towards attributing a pitchfork-like form to the relevant bifurcation diagram. However, it is important to keep in mind that the stability of this solution is also reversed in comparison to the one with G<0. Moreover, the linear and quadratic terms that we will encounter below within the system's reduced dynamics will also be reminiscent of a transcritical normal form].

Returning to the stationary problem, when  $|\tau| \to \infty$ , equation (12) simplifies into the stationary ordinary differential equation (ODE):

$$-\frac{\mathrm{d}^3 w}{\mathrm{d}\xi^3} - \frac{\mathrm{d}w^p}{\mathrm{d}\xi} + G\left(\frac{2w}{p-1} + \xi \frac{\mathrm{d}w}{\mathrm{d}\xi}\right) + \frac{\mathrm{d}w}{\mathrm{d}\xi} = 0. \tag{13}$$

For our numerical computations throughout this work, we consider a symmetric and finite spatial domain [-L, L], where  $L \gg 1$ . The bounded nature of the computational domain necessitates the implementation of boundary conditions (BCs) which in this work are:

$$\frac{2Gw}{p-1} + (G\xi + 1)\frac{\partial w}{\partial \xi}\bigg|_{|\xi|=L} = 0,$$
(14a)

$$\left. \frac{\partial^2 w}{\partial \xi^2} \right|_{\xi = L} = 0. \tag{14b}$$

It is important to highlight here that these BCs bear similarities to the ones employed in [16], yet incorporate the role of the blow-up rate G explicitly. Our subsequent analysis will illustrate that they accurately encapsulate the asymptotic behaviours of the self-similar profiles that we compute in this work. It is noteworthy that based on the aforementioned BCs, and considering G < 0, the solution's slow algebraic decay manifests to the left of its peak, while the more rapid

exponential decay transpires on its right side (consistent with the profiles in [16]). If we perform the transformation  $G \mapsto -G$  and  $\xi \mapsto -\xi$  in equations (13) (which retains its invariance) and (14a)–(14b), these decaying behaviours interchange, aligning with the numerical findings reported in [24].

It has been reported that G is a dynamic variable, gradually approaching a constant value as  $|\tau| \to \infty$ , which needs to be determined in a self-consistent manner for a given value of p. To achieve this, following the methodologies outlined in the works of [31, 35, 36] (and references therein), we 'close' the systems of equations (12) and (13) (both subject to the BCs of equations (14a)–(14b)) by introducing a pinning condition. This lifts the degeneracy of the one-parameter infinity of available (self-similarly rescaled) solutions and selects a unique one among them, while at the same time providing the appropriate value of G. In our subsequent analysis and computations detailed in the forthcoming sections, and without any loss of generality, we enforce a 'pinning condition' in the form of an internal BC:

$$\left. \frac{\partial w}{\partial \xi} \right|_{\xi=0} = 0. \tag{15}$$

This condition facilitates the unique determination of a self-similar solution characterised by a constant value of G. By constraining the wave's value (or its derivatives) at a specific point, as exemplified in equation (15), one can effectively compute the pertinent unique solution which in this case is prescribed to be peaked (i.e. features a maximum) at the origin.

We conclude this section by outlining the primary framework of the gKdV spectral stability problem. We investigate the linear stability of a self-similar solution  $w(\xi)$  (characterised by  $G \neq 0$ ), which remains stationary in the self-similar frame. This study involves considering the ansatz:

$$\widetilde{w}(\xi,\tau) = w(\xi) + \delta v(\xi) e^{\lambda \tau}, \quad \delta \ll 1,$$
(16)

where  $(\lambda, \nu(\xi))$  denotes the eigenvalue-eigenvector pair. Upon inserting equation (16) into equation (12), we arrive at order  $\mathcal{O}(\delta)$  at the eigenvalue problem:

$$\lambda v = \mathcal{L}v,\tag{17}$$

where the operator  $\mathcal{L}(\cdot)$  is defined as:

$$\mathcal{L}(\cdot) := \frac{2G}{p-1} - p(p-1)w^{p-2}\frac{dw}{d\xi} + \left(G\xi + 1 - pw^{p-1}\right)\frac{d}{d\xi} - \frac{d^3}{d\xi^3},\tag{18}$$

representing the linearisation operator whose eigenvalues we compute. Notably, the stability characteristics of TWs (over p) can also be explored using equation (18), albeit with G=0. For all cases, i.e. G=0 or  $G\neq 0$ , the eigenvalues  $\lambda=\lambda_r+\mathrm{i}\lambda_i$  of the linear operator presented in (18) provide information about the stability of the computed waveforms. The presence of a non-zero positive real part in an eigenvalue, i.e.,  $\lambda_r>0$ , indicates linear instability in the computed solution. Conversely, the absence of eigenvalues with a positive real part suggests (linear) stability. It is also important to appreciate the 'dual' character of the relevant linearisation setting, similarly to what was discussed in the NLS case in [31, 36]. Namely, the relevant problem is a Hamiltonian one for G=0, featuring the corresponding eigenvalue symmetries (i.e., for each complex  $\lambda$ , each of  $-\lambda$ , the complex conjugate  $\lambda^*$  and  $-\lambda^*$  are all eigenvalues). On the other hand, for  $G\neq 0$ , the problem is genuinely non-conservative, and only the symmetry of  $\lambda\to\lambda^*$  will be present in the corresponding spectra. This renders the relevant

bifurcation problem especially interesting from a mathematical point of view, given its mixed Hamiltonian-dissipative type.

In the upcoming section on our numerical findings, we will delve into the challenges posed by the eigenvalue problem in equation (17) addressing them as we compute both the point and the continuous spectrum of the operator  $\mathcal{L}$  (as defined in equation (18)).

### 3. Computational and theoretical results

We begin our discussion with a brief presentation of the spectra of the better-known case of the TWs, i.e. for G=0 across various nonlinearity exponents, p, as we consider the relevant bifurcation problem. Subsequently, we delve into a comprehensive analysis of the existence and spectral properties of self-similar solutions, characterised by  $G \neq 0$ , and their asymptotic behaviour (for  $|\xi| \gg 1$ ) within the co-exploding frame. We also present the normal form that describes the bifurcating branch of self-similar solutions from the solitary wave branch, at p=5.

#### 3.1. The TW case and spectra: G = 0

Let us first focus on the soliton case corresponding to G=0 in equations (13) and (17). While the analytical expression of the TW solution is available (see equation (4)), we numerically compute the solution to equation (13) subject to the BCs given by equations (14a)–(14b). Notice that for the present branch of G=0, the latter amount to a homogeneous Neumann BC pair plus the vanishing of the second derivative on one of the sides (given the need for three such conditions). This approach is taken to ensure that the computation of the TW's spectrum is conducted on the same computational grid and with the same spatial discretisation as used for solving the root-finding problem of equation (13). This strategy eliminates local truncation errors (LTEs) that could arise if we had directly plugged the TW solution into the eigenvalue problem of equation (17), which might have led to potential perturbations of the eigenvalues. In this study, we adopt a finite volume discretisation approach. For discretizing the computational domain  $\xi \in [-L, L]$ , we have chosen equidistant nodes with a spacing of  $\delta \xi = 0.001$ . We compare the results for different values of L as discussed below.

We use the TW solution from equation (4) as an initial guess within a Newton algorithm for p=2, progressively conducting continuation steps across varying values of p up to p=5.8. At each continuation step, we compute the spectrum of the operator  $\mathcal{L}$  (cf equation (18)) associated with the eigenvalue problem defined by equation (17) for G=0, corresponding to the solitonic branch. We compute our numerical spectra using MATLAB's eigs function. During this computation, we pay particular attention to the dominant unstable (real) eigenvalue. In figure 1, we present the variation of this eigenvalue with respect to p, showcasing the results from p=4.2 to 5.8. The depicted figure clearly illustrates that the TW remains stable until p=5, as evidenced by the absence of an unstable eigenmode with a positive real part. However, as we push beyond the threshold of p=5, instability sets in, accompanied by the emergence of a positive real eigenmode. This observation corroborates the findings in [15] for the gKdV equation.

We finalise our discussion on the spectra of TW solutions to the gKdV by presenting their full spectra  $\lambda = \lambda_r + \mathrm{i}\lambda_i$  for two distinct values of p, considering various domain half-widths, L, as depicted in figure 2 (refer to the corresponding legends). The left panel corresponds to the subcritical case of p = 4.9, while the right panel pertains to the supercritical case of p = 5.1, where the TW solution is unstable. Some observations can be made based on the

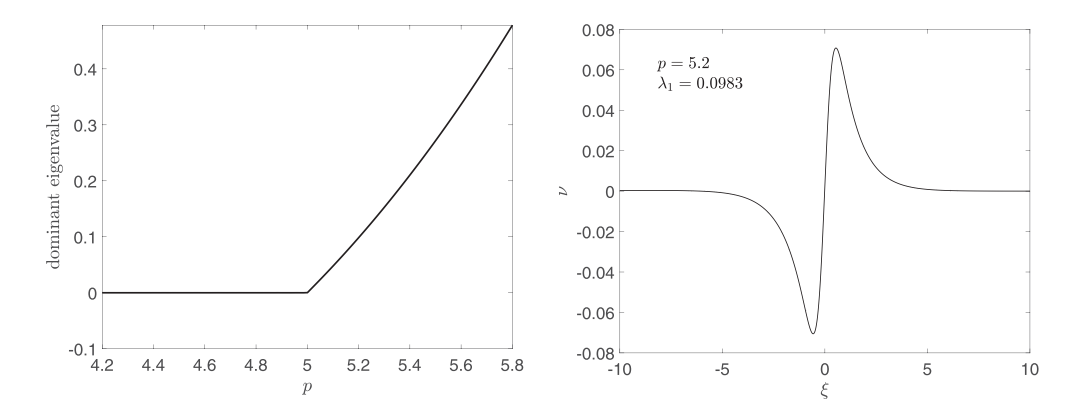


**Figure 1.** (left panel) The variation of the largest real, i.e. dominant eigenvalue of the TW solution (cf equation (4)) over the nonlinearity exponent p. The TW becomes spectrally unstable for p > 5. The right panel shows the corresponding eigenvector, v, for the dominant eigenvalue ( $\lambda_1 = 0.0983$ ) of the TW solution for p = 5.2.

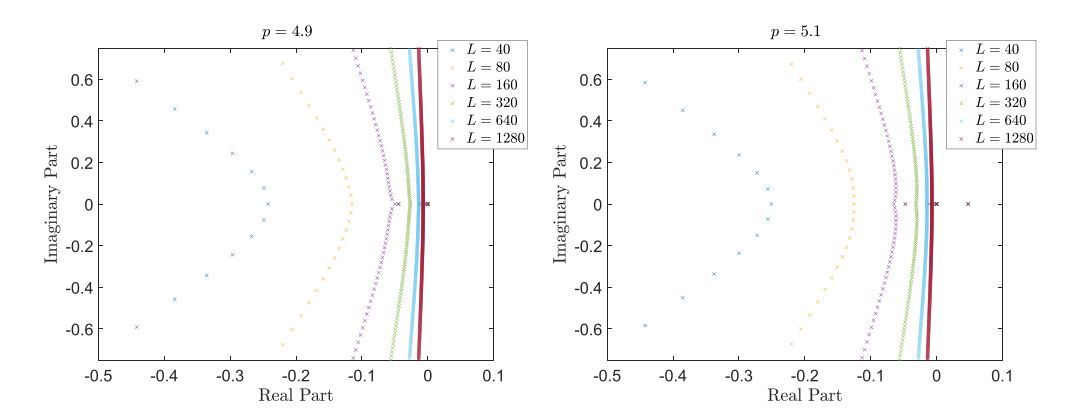


**Figure 2.** Spectra of  $\mathcal{L}$  (cf equation (18)) associated with the TW branch of figure 1. The left and right panels of the figure showcase the full spectra of TWs for p=4.9 (subcritical case) and p=5.1 (supercritical case), and for various values of the domains' half-width L. We have performed a convergence test of the spectrum by starting from L=40 and doubling it each time up to L=1280 (see the legends therein in both panels). As the infinite domain case is progressively approached, the wedge-like spectrum in both panels starts aligning with an almost vertical spectrum that is proximal to the imaginary axis.

information presented in figure 2. In both panels, the continuous spectrum is notably influenced by the size of the domain. For relatively modest L values, such as L=40 and L=80, the continuous spectrum appears to take on a wedge-like shape. However, as the domain size increases, particularly for L=640 and L=1280, this shape transforms into a nearly vertical (for the scale of the graph) distribution approaching the imaginary axis and thus suggesting the asymptotic form thereof. In addition, the symmetry mode, accounting for spatial translations, becomes increasingly distinguishable and well-resolved with larger L values in our numerical computations, aligning with the expected behaviour. It is worth noting that the unstable mode that emerges for p>5 (also observed in figure 1) remains unaffected by changes in L. Note that the wedge-like spectra that we find here for the TWs are because of the imposition of BCs of

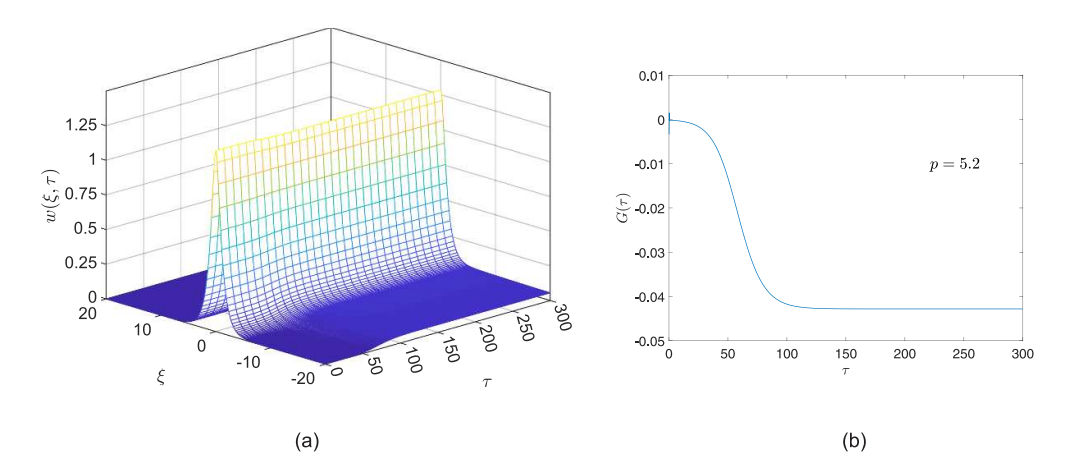


**Figure 3.** Self-similar dynamics of equation (12) for p=5.2. The TW solution of equation (4) was used as an initial condition in the simulation. Panel (a) depicts the evolution of the TW solution towards the self-similar profile. In panel (b), the temporal evolution of the blow-up rate  $G(\tau)$  is monitored. Note that the self-similar dynamics converges to a 'steady-state' solution of the co-exploding frame when  $\tau > 100$ .

equations (14a)–(14b) being themselves consonant with those of the self-similar solutions that follow. If we were to impose, e.g., periodic BCs, the spectra of the TWs would be respecting the Hamiltonian symmetry and structure of the model. As a result, the spectrum would be fully on the imaginary axis for p < 5 and featuring only a real pair (in addition to encompassing the entire imaginary axis) for p > 5.

# 3.2. Existence of self-similar solutions: $G \neq 0$

The observed instability of the TW as shown in figure 1 for p > 5 is consistent with the subsequent self-similar blow-up of the TW, a phenomenon already discussed in section 2. We now proceed with the computation of self-similar solutions for the gKdV (equation (1)). As previously reported in section 2, solutions that exhibit self-similarity in the renormalised / coexploding frame translate to stationary solutions of equation (12). By directly simulating the initial-boundary value problem (IBVP) of equations (12) and (14a)–(14b) along with the pinning condition specified by equation (15),  $w(\xi, \tau) \mapsto w(\xi)$  as  $\tau \to \infty$ . Here,  $w(\xi)$  is a solution satisfying equation (13).

This way, the self-similar profile can be determined by utilizing the TW solution as an initial condition, specifically for a value of p where the TW exhibits instability. We integrate equation (12) in (the renormalised) time using a backward Euler method [38]. We have also tested our time integration algorithm by comparing its outcomes with those obtained from MATLAB's ode23t function, showing a high degree of agreement. Throughout the time integration process, we consistently impose the pinning condition defined in equation (15) at each time step. This permits the computation of the rate of width change, G (or blow-up rate) as a function of  $\tau$ , as illustrated in equation (8). The results of this simulation are depicted in figure 3, specifically for p = 5.2. The left panel of the figure illustrates the spatio-temporal evolution of  $w(\xi,\tau)$  within the renormalised frame, while the right panel tracks the variation of the blow-up rate, G, with  $\tau$ . As evident from the panels, once a transient time window  $\approx (0,100]$  elapses, the self-similar dynamics tends towards a stationary profile (as observed

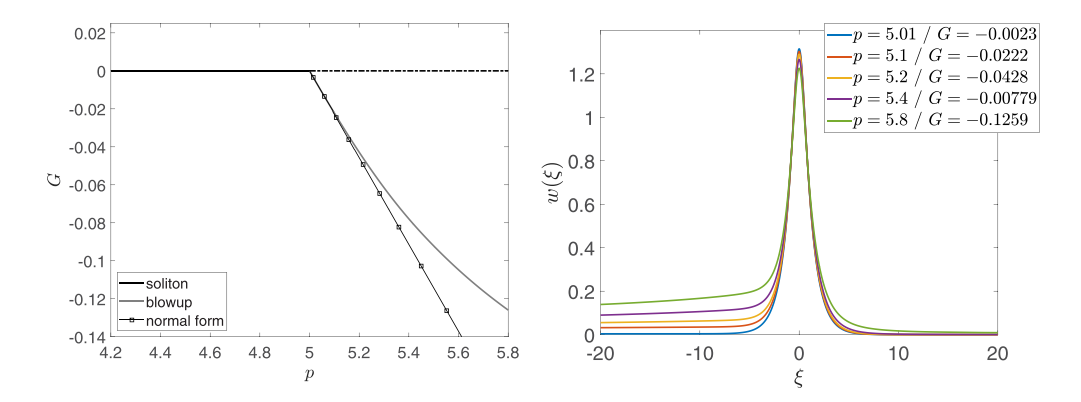


**Figure 4.** Existence results of self-similar solutions to the gKdV obtained numerically. In the left panel, the solid grey line corresponds to the dependence of the blow-up rate G on p for the self-similar branch. The black line with rectangles corresponds to the results obtained from the normal form (steady state solutions of equation (65)). The solitonic branch with G=0 is overlaid in the panel, and shown with a solid black line (for its stable portion), with the dashed part corresponding to the unstable segment of the solitonic branch. The right panel presents a few self-similar profiles for different values of p (and G). For their values, see the legend therein.

in the left panel). Simultaneously, the blow-up rate, G, reaches a constant, negative value (as indicated in the right panel). This stationary nature of the self-similar dynamics permits the accurate computation of the self-similar profile in accordance with equation (13). In particular, we extract the terminal solution at  $\tau=300$  from the dynamics and employ it, in conjunction with the asymptotic value of G, as an initial guess for a Newton method, which rapidly converges. It is also important to highlight here that the relaxational nature of the dynamics predisposes us towards the expected dynamical stability of such a self-similarly collapsing state

The alternative, more computationally accurate approach adopted in our work for the numerical computation of self-similar solutions is by directly tackling the boundary value problem equation (13) with BCs of equations (14a)–(14b) and the pinning condition described in equation (15). Upon using either the above mentioned initial guess or a slightly perturbed TW for p > 5, along the most unstable eigenvector (as described in equation (16)—see also right panel of figure 1), we obtain the corresponding self-similar waveform for the respective p. Upon achieving convergence through the Newton's method (either by employing this approach or the one mentioned earlier), we proceed with parametric continuation [39] across the nonlinearity exponent, p. This step enables the full tracing of the branch of self-similar solutions.

Displayed in figure 4 are our numerical findings regarding the existence of self-similar solutions to the gKdV equation (as defined in equation (13)). In the left panel of the figure, the dependence of G on p for the self-similar branch (G < 0) is illustrated by the grey line, while the solid black line represents the soliton (TW) branch. The dashed black line segment signifies the unstable nature of the solitary wave solutions for p > 5. On the right panel, the numerically obtained self-similar profiles for various p values are presented, along with the corresponding blow-up rates, G, indicated in the legend. Notably, the profiles presented in this panel exhibit identical characteristics to those reported in [16]. Specifically, the solutions display a power-law decay on the left side and a rapid (exponential) decay on the right side, with respect to the peak located at the origin. Through the application of the transformation

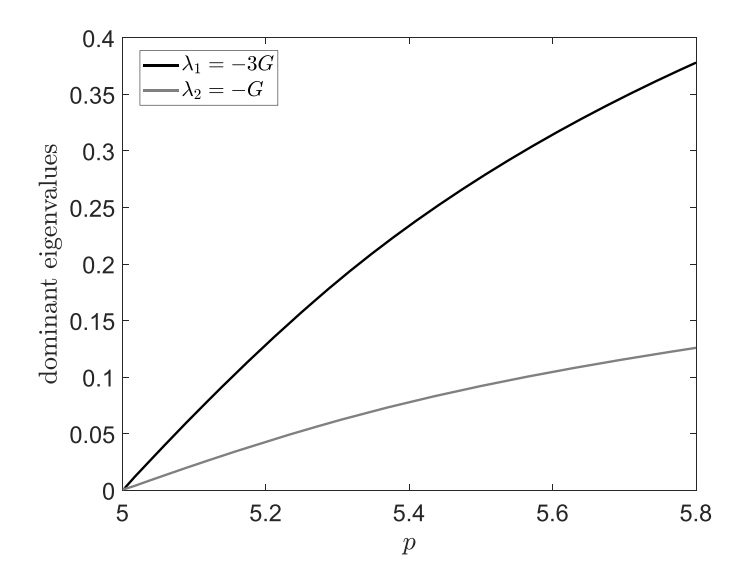


**Figure 5.** The dependence of the 2 unstable eigenvalues as a function of p. Note that those are precisely located at  $\lambda_1 = -3G$  and  $\lambda_2 = -G$ .

 $G \mapsto -G$  and  $\xi \mapsto -\xi$ , we observe that the regions capturing the asymptotic behaviours of the solutions are indeed exchanged (results not displayed). The resulting profiles align with those presented in [24] under this transformation.

#### 3.3. Spectral analysis of self-similar solutions: G < 0

We now shift our focus to the spectral analysis of the self-similar solutions within the context of the gKdV equation. In this pursuit, we recall the eigenvalue problem outlined in equation (17), along with its corresponding operator,  $\mathcal{L}$ , as presented in equation (18). During each step of the continuation method, which we have employed to trace the self-similar branch (G < 0), we compute the spectrum of the operator,  $\mathcal{L}$ . Our ensuing analysis will be divided into two components: one centred around the point spectrum, and the other concerning the continuous spectrum. Regarding the point spectrum, our findings reveal the existence of four real eigenvalues that can be systematically traced. Among these four, two eigenvalues are positive, denoted as  $\lambda_1$  and  $\lambda_2$ , with  $\lambda_1 > \lambda_2$ . The remaining two eigenvalues are negative, designated as  $\lambda_{-1}$  and  $\lambda_{-2}$ , with  $\lambda_{-1} > \lambda_{-2}$ .

Let us begin our analysis with the two positive eigenvalues that pertain to *apparent* instabilities in the co-exploding frame. We find that these eigenvalues are precisely situated at  $\lambda_1 = -3G$  and  $\lambda_2 = -G$ , a fact readily observed in figure 5. This is true up to exponentially small corrections in the size of the domain which are imperceptible over the scales shown and for the choices of L made herein. Accompanying these eigenvalues, we also present the explicit forms of their associated eigenfunctions (for the infinite domain problem). Specifically, the eigenvector associated with  $\lambda_1 = -3G$  is:

$$v(\xi) = \frac{2}{p-1}w + \xi w_{\xi} + \frac{1}{G}w_{\xi},\tag{19}$$

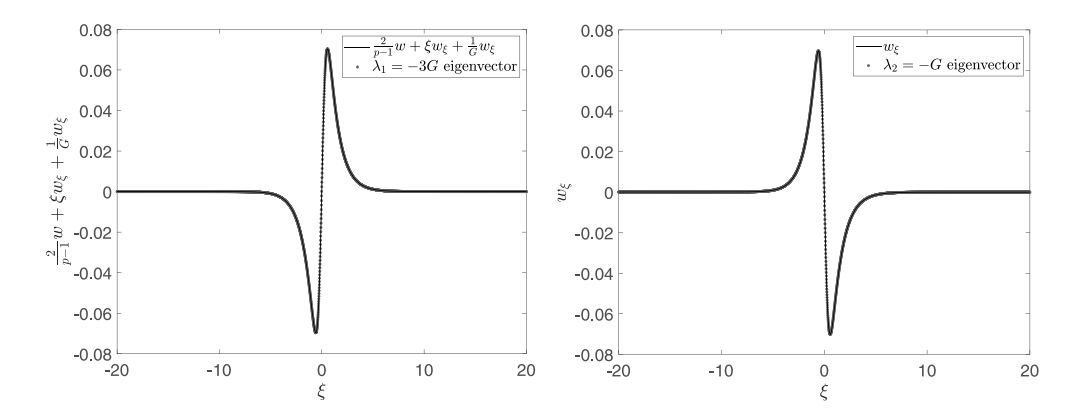


**Figure 6.** Comparison of (the practically identical) exact and numerically obtained eigenvectors shown with a black solid line and grey dots, respectively, for p = 5.2. The left panel presents the eigenvector associated with  $\lambda_1 = -3G$  and the scaling invariance (cf equation (19)) whereas the right panel depicts the one associated with  $\lambda_2 = -G$  and translational invariance (cf equation (20)).

where the subscript indicates differentiation with respect to  $\xi$ . Similarly, when considering  $\lambda_2 = -G$  the (exact, in the infinite domain limit) eigenvector takes the form:

$$v\left(\xi\right) = w_{\xi}.\tag{20}$$

This latter eigenvector is associated with the translational invariance of the problem, while the former is connected with the scaling symmetry and the associated invariance. Figure 6 presents a comparison between the exact eigenvectors derived from equations (19) and (20) (depicted as solid black lines) and the numerically computed counterparts (depicted as gray dots). For the sake of illustration, we choose a specific value for the nonlinearity exponent, namely p=5.2. It is evident from the panels of the figure that the two sets of eigenvectors exhibit a remarkable agreement with their corresponding theoretical prediction for the choices of L depicted herein.

Let us now delve into the discussion concerning the two aforementioned negative real eigenvalues, namely  $\lambda_{-1}$  and  $\lambda_{-2}$ , which we systematically trace during our computations. The eigenvalue,  $\lambda_{-1}$ , aligns fairly closely with G/2, while  $\lambda_{-2}$  displays oscillations centred around 2G. The left panel of figure 7 illustrates these behaviours, depicting the dependence of these negative real eigenvalues on the nonlinear exponent, p with solid blue (accompanied by open circles) and red (with open squares) lines, respectively. In the same panel, dashed-dotted red and blue lines correspond to the values of G/2 and 2G as functions of p, included for comparison. Examining the left panel, we observe that while the eigenvalue,  $\lambda_{-1}$ , remains consistently proximal to the prediction of G/2 (see also details below) starting from its emergence at p=5, it does exhibit small oscillations that gradually increase in amplitude as p grows. Similarly, the eigenvalue,  $\lambda_{-2}$ , displays more vigorous oscillatory behaviour around 2G (indicated by the solid red line with open squares). Furthermore, the panel showcases the behaviour of the third and fourth largest negative eigenvalues, denoted as  $\lambda_{-3}$  and  $\lambda_{-4}$ , depicted with solid orange (with open triangles) and purple (with stars) lines, respectively. Similar to  $\lambda_{-2}$ , these eigenvalues also experience oscillations around 2G, which get amplified as p increases. It is worth noting that these oscillations are a consequence of the finite domain size employed in our analysis, and we will delve into a systematic analysis of these oscillations later. Illustrating the effect of the domain size, the right panel of figure 7 compares the dependence of  $\lambda_{-4}$  on p for

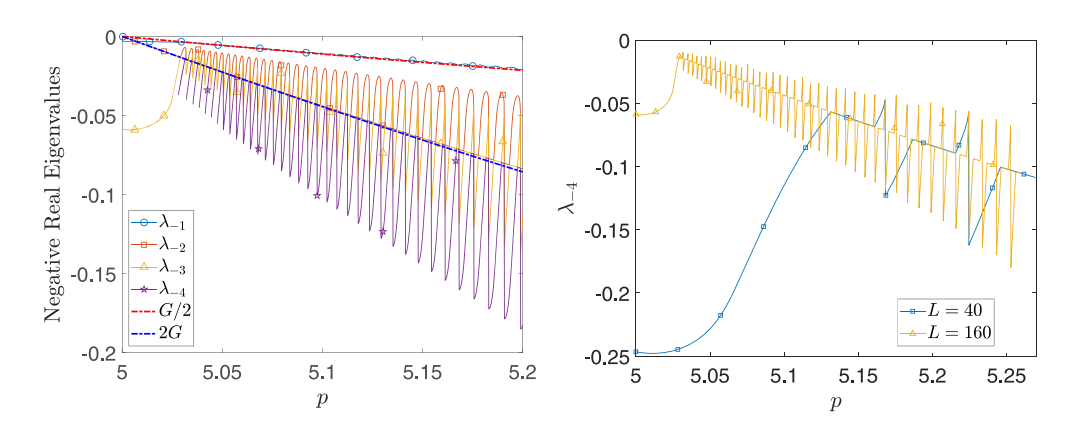


**Figure 7.** Continuation of figure 5 but now for the largest negative real eigenvalues. The left panel presents the variation of the 4 largest negative real eigenvalues,  $\lambda_{-1} > \lambda_{-2} > \lambda_{-3} > \lambda_{-4}$  over p (see the legends therein), and for (domain half-width) L=160. In particular,  $\lambda_{-1}$  oscillates around G/2 (red dashed-dotted line) whereas  $\lambda_{-2,-3,-4}$  around 2G (depicted with blue dashed-dotted line). The right panel highlights the finite-size domain effect by showcasing the variation of  $\lambda_{-4}$  over p, and for L=40 (solid blue line with open squares), and L=160 (solid orange line with open triangles).

two different domain half-widths, specifically L=40 and L=160. The solid blue line (with open squares) and orange line (with open triangles) represent  $\lambda_{-4}$  for L=40 and L=160, respectively. This comparison highlights that as the domain half-width increases from 40 to 160, the real part of  $\lambda_{-4}$  decreases (in terms of its absolute value) from its initial value at p=5. Additionally, the oscillations in the eigenvalue are discernible at lower values of p for the larger domain size (L=160), though  $\lambda_{-4}$  continues to oscillate around 2G in both cases.

The finite-size effects, whose influence we have already seen in part, leave their imprint on the continuous spectrum of self-similar solutions as well. The left panel of figure 8 depicts the spectrum of the operator  $\mathcal{L}$  (cf equation (18)) for a specific value of p = 5.1, as it varies with the domain's half-width, L (again, by doubling L each time as we performed in figure 2). However, the continuous spectrum in this context presents distinctive attributes compared to the TW case. The continuous spectrum can be split into two segments: an almost-vertical portion situated close to  $G \approx -0.022$ , and a wedge-like portion, reminiscent of the one observed in the TW case. Upon increasing L, we note that the nearly-vertical segment of the continuous spectrum remains relatively consistent, gradually converging toward a real part of the relevant spectrum equal to G. It is relevant to note here that this feature is reminiscent of the continuous spectrum in the NLS case [36]. Concurrently, the wedge angle associated with the other portion of the continuous spectrum widens, leading to a transformation of the wedge-like section into an almost-vertical line parallel to the imaginary axis. Meanwhile, the distance between this almost-vertical section of the spectrum and the imaginary axis expands as p increases. This is illustrated in the right panel of figure 8, where a comparison of the spectra between p = 5.1 and p = 5.5 is presented using blue and red crosses, respectively. Nevertheless, as will be discussed below, this portion of the spectrum is *not* well-resolved. More specifically, we will argue that this segment is extremely ill-conditioned and, in reality, it is supposed to lie on the negative real axis. It is noted that, similarly to the p = 5.1 case, the vertical section of the spectrum at p = 5.5 aligns precisely with  $G \approx -0.0922$ .

We now proceed with the analytical approximation of both the continuous and point spectrum of the operator,  $\mathcal{L}$ , by using the Wentzel-Kramers-Brillouin (WKB) method [40]. We

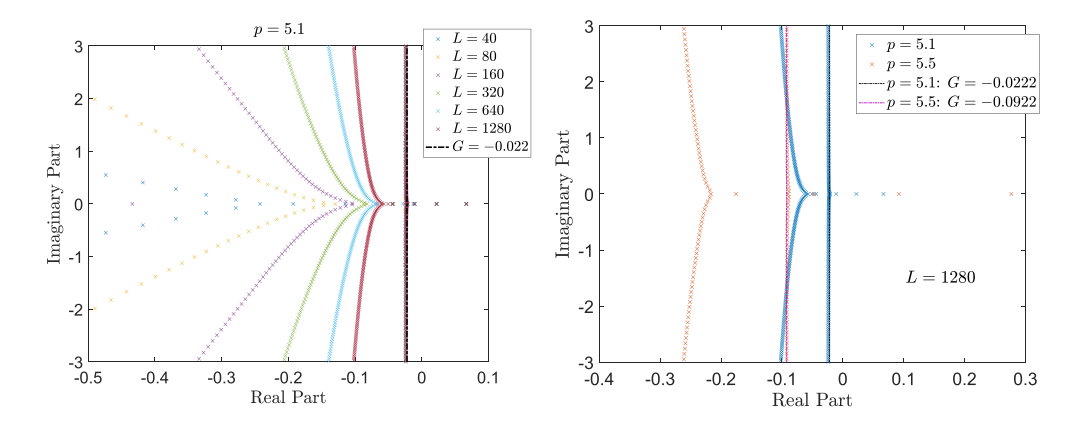


Figure 8. Same as figure 2 but for the self-similar branch. In the left panel, we present spectra of  $\mathcal{L}$  (cf equation (18)) with p=5.1 as functions of the domain size L (see the legend therein). We employ a similar convergence analysis over L as we performed in figure 2. Interestingly, the spectrum involves two parts: a vertical part that lands exactly on  $G \approx -0.022$  (see also the dashed-dotted line, representative of this value), and a wedge-like one that is morphed into a vertical spectrum as L increases, i.e. as we approach the infinite domain case; yet this portion of the spectrum will be argued to not be well-resolved in what follows. The right panel of the figure, considers L=1280, and compares the spectrum of two self-similar solutions with p=5.1 (blue crosses) and p=5.5 (red crosses). The dashed-dotted black and purple lines are introduced to high-light the location of the vertical parts of the spectrum at  $Re(\lambda) \approx G$  (see the legend).

suppose that we are close to the bifurcation point, so that p is close to 5 and G is close to zero. We will see in section 3.4 that the steady self-similar solution comprises an inner region in which  $\xi = O(1)$ , and an outer region in which  $\xi = O(1/\varepsilon)$ , where  $\varepsilon = -G > 0$  measures the distance from the bifurcation point, so that p-5 is proportional to  $\varepsilon$ . This inner-outer structure is inherited by the eigenvalue problem. However, we will find that the spectral properties are mainly determined by the outer region. Thus we adopt a rescaling into the outer region by introducing the transformations:

$$y = \varepsilon \xi, \quad G = -\varepsilon, \quad \varepsilon > 0.$$
 (21)

After substituting equations (21) into equations (17) and (18), we obtain

$$\frac{\lambda}{\varepsilon}v = -\varepsilon^2 \frac{\mathrm{d}^3 v}{\mathrm{d}y^3} - p \frac{\mathrm{d}}{\mathrm{d}y} \left(vw^{p-1}\right) - \left(\frac{2v}{p-1} + y \frac{\mathrm{d}v}{\mathrm{d}y}\right) + \frac{\mathrm{d}v}{\mathrm{d}y}.\tag{22}$$

Since  $w^{p-1}$  is exponentially small in the outer region it may be neglected. Expanding p as  $p = p_0 + \varepsilon p_1 + \cdots$  (with  $p_0 = 5$ ), we obtain:

$$\frac{\lambda}{\varepsilon}v + \varepsilon^2 \frac{\mathrm{d}^3 v}{\mathrm{d}y^3} - \frac{\mathrm{d}v}{\mathrm{d}y} = -\left(\frac{v}{2} + y\frac{\mathrm{d}v}{\mathrm{d}y}\right) + \frac{\varepsilon p_1 v}{8} + \cdots$$
 (23)

Subsequently, we introduce the WKB ansatz:

$$v \sim A e^{\phi/\varepsilon}, \quad \varepsilon \downarrow 0,$$
 (24)

where  $\phi(y)$  represents the phase and A(y) corresponds to the slowly varying amplitude. Equating coefficients of powers of  $\varepsilon$  at orders  $\mathcal{O}(\varepsilon^{-1})$  and  $\mathcal{O}(1)$  gives, respectively,

$$\lambda + (\phi')^3 + (y - 1)\phi' = 0, (25a)$$

$$3A'(\phi')^{2} + 3A\phi'\phi'' - A' = -\frac{A}{2} - yA', \tag{25b}$$

the latter of which can be further rearranged as

$$\frac{A'}{A} + \frac{1}{2} \frac{6\phi'\phi'' + 1}{3(\phi')^2 - 1 + y} = 0, (26)$$

and subsequently integrated with respect to y, yielding

$$A = \frac{1}{\left(3\left(\phi'\right)^2 - 1 + y\right)^{1/2}},\tag{27}$$

where we have set the constant of integration to unity. Since equation (25a) is a cubic, there are three distinct WKB solutions, which we denote by  $v_i \sim A_i e^{\phi_i/\epsilon}$ , with i = 1, 2, 3. We choose these so that for real y, the phase functions have asymptotic behaviour

$$\phi_1' \sim (-y)^{1/2}, \qquad \phi_2' \sim -(-y)^{1/2}, \qquad \phi_3' \sim -\frac{\lambda}{y} \qquad \text{as } y \to -\infty.$$
 (28)

We find that there are turning points at

$$y = 1 - 3\left(\frac{\lambda}{2}\right)^{2/3}.\tag{29}$$

Because of the third root, there are three turning points, which we label as  $y_A$ ,  $y_B$  and  $y_C$ .

Naively we might now try to approximate an eigenfunction as a linear combination of  $v_1$ ,  $v_2$  and  $v_3$ . However, in doing so it is crucial to understand both (i) how the WKB solutions are permuted when circling a turning point because of the Riemann surface associated with the function  $\phi$  (turning points are branch points of  $\phi$ ), and, (ii) how the coefficients in such a linear combination will change discontinuously across the Stokes lines associated with each of the turning points [41–43]. The following analysis of the eigenvalue problem uses a similar approach to that in [44].

A typical Stokes line picture is shown in figure 9. When the turning point  $y_A$  is encircled, the phase  $\phi_1$  becomes  $\phi_3$  and vice versa. Similarly, as the turning point  $y_B$  is encircled,  $\phi_2$  becomes  $\phi_3$ , and vice versa, while when the turning point  $y_C$  is encircled,  $\phi_1$  switches places with  $\phi_2$ . For definiteness we introduce branch cuts across which these interchanges in labels take place (see figure 9). Stokes lines in figure 9 are indicated by solid lines. Across each of the lines a dominant WKB solution will switch on a subdominant WKB solution (i.e. there will be a change in the coefficient of the subdominant solution proportional to the coefficient of the dominant solution). The relevant dominant/subdominant WKB solutions depend on the turning point at which the Stokes lines originate. Also shown in figure 9 are anti-Stokes lines (dashed) across which the dominance of two WKB solutions switches. Finally, the spirals around each turning point illustrate one of the possible local branch point/Stokes switching structures.

Let us explain these by considering the diagram in the vicinity of the turning point  $y_C$ , for example, with a solution in which only the WKB solution  $v_1$  is present to the left of the turning

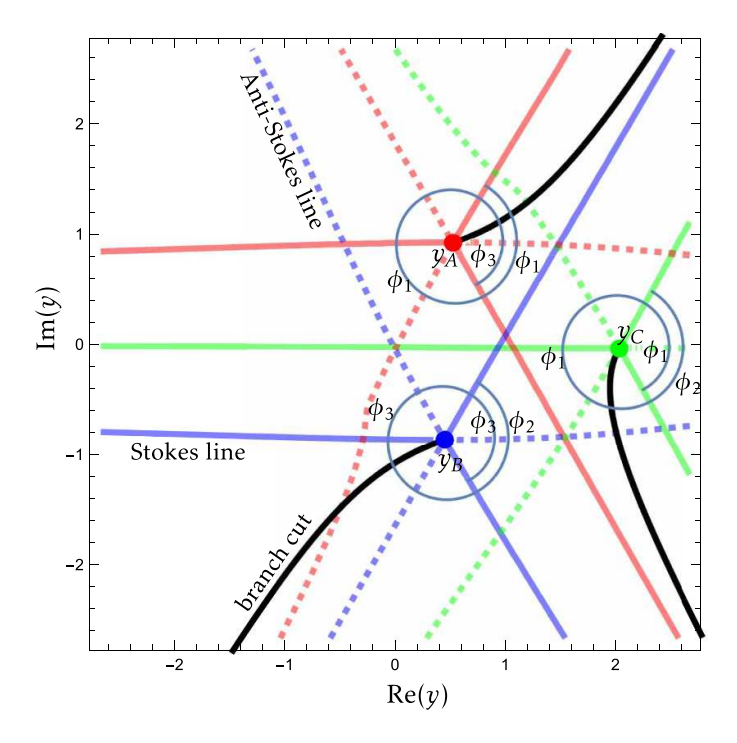


**Figure 9.** Stokes lines (solid) and anti-Stokes lines (dashed) when  $\lambda \approx -0.02537 - 0.401$ i. Solid black lines are branch-cuts of the phase function  $\phi$ . Three turning points  $y_A$ ,  $y_B$  and  $y_C$  are indicated. Each is a square root branch point of  $\phi$ . The local Riemann surface structure in the vicinity of each branch point is indicated by the spirals, which shows which branches of  $\phi$  are turned on/off across the Stokes lines.

point. There is a possible Stokes line close to the negative real axis but it is not active because  $\phi_1$  is subdominant to  $\phi_2$  there. As the turning point is encircled clockwise we first cross the anti-Stokes line at which  $\phi_1$  becomes the dominant exponential, followed by another Stokes line. Since  $\phi_1$  is now dominant, a multiple of  $\phi_2$  is turned on. Proceeding clockwise we cross another anti-Stokes line close to the positive real axis across which  $\phi_1$  and  $\phi_2$  again exchange dominance. We then meet another Stokes line, at which  $\phi_2$  is the dominant exponential. At this Stokes line there is a change in the coefficient of  $v_1$ —in fact the change is such that the coefficient is zero after the Stokes line is crossed, so that only  $\phi_2$  remains. We then cross the branch cut, so that  $\phi_2$  becomes  $\phi_1$  and we return to where we started.

The approximate eigenvalue condition stipulates that the anti-Stokes line emanating from one of the turning points intersects the right-hand boundary (see figure 9, for which the anti-Stokes line from  $y_C$  passes through the right-hand boundary). This gives three branches of eigenvalues (one for each turning point), which are roughly (A)  $\operatorname{Re}(\lambda) \approx G$ ,  $\operatorname{Im}(\lambda) > 0$ ; (B)  $\operatorname{Re}(\lambda) < G$ ,  $\operatorname{Im}(\lambda) = 0$ ; and (C)  $\operatorname{Re}(\lambda) \approx G$ ,  $\operatorname{Im}(\lambda) < 0$ .

To see why this should be the case we first observe that, as we move into the domain from the left-hand boundary, the WKB approximations  $v_3$  and  $v_2$  decay exponentially, while  $v_1$  grows exponentially. Let us start by describing branch (C). We proceed to construct an eigenfunction as follows: The left-hand BC can be satisfied by adding a multiple of  $v_3$  and  $v_2$ . Since  $v_2$  exhibits a stronger decay, it can be safely disregarded at the right-hand boundary. To satisfy the conditions at the right-hand boundary we need some more degrees of freedom. We can add

a multiple of  $v_1$  without affecting the left-hand boundary—since  $v_1$  is exponentially larger on the right than the left. We choose our normalisation of the eigenfunction to fix this multiple of  $v_1$  to unity (choosing  $\phi_1(y_C) = 0$ ). Let us now determine the form of the eigenfunction at the right-hand boundary, taking into account the Stokes switchings. The solution  $v_1$  will turn on a multiple of  $v_2$  due to the turning point  $y_C$ . The Stokes multiplier is -1 (if we set  $\phi_2(y_C) = 0$ ). There are also Stokes switchings associated with  $y_A$  and  $y_B$ , but we can see from figure 9 that the functions switched on are exponentially subdominant up to the boundary (since the anti-Stokes line has not been crossed). As a result, the eigenfunction takes the following form near the right-hand boundary:

$$v = aA_3 e^{\phi_3/\varepsilon} - A_2 e^{\phi_2/\varepsilon} + A_1 e^{\phi_1/\varepsilon}, \tag{30}$$

where  $\phi_1$  and  $\phi_2$  are both zero at  $y = y_C$  (the zero of  $\phi_3$  can be chosen arbitrarily since changing it simply changes the coefficient a). Subsequently, using equation (30), we can express the first-and second-order derivatives of v with respect to y near the right-hand boundary as:

$$v' = \frac{1}{\varepsilon} \left( a\phi_3' A_3 e^{\phi_3/\varepsilon} - A_2 \phi_2' e^{\phi_2/\varepsilon} + A_1 \phi_1' e^{\phi_1/\varepsilon} \right) + \cdots, \tag{31a}$$

$$v'' = \frac{1}{\varepsilon^2} \left( a \left( \phi_3' \right)^2 A_3 e^{\phi_3/\varepsilon} - A_2 \left( \phi_2' \right)^2 e^{\phi_2/\varepsilon} + A_1 \left( \phi_1' \right)^2 e^{\phi_1/\varepsilon} \right) + \cdots . \tag{31b}$$

Now imposing (14a) at  $y = \varepsilon L$ , the coefficient a can be determined at leading-order as

$$a = \frac{A_2 \phi_2' e^{\phi_2/\varepsilon} - A_1 \phi_1' e^{\phi_1/\varepsilon}}{\phi_3' A_3 e^{\phi_3/\varepsilon}},\tag{32}$$

which reduces equation (31b) at  $y = \varepsilon L$  to

$$v'' = \frac{1}{\varepsilon^{2}} \left( \frac{A_{2} \phi_{2}' e^{\phi_{2}/\varepsilon} - A_{1} \phi_{1}' e^{\phi_{1}/\varepsilon}}{\phi_{3}' A_{3} e^{\phi_{3}/\varepsilon}} (\phi_{3}')^{2} A_{3} e^{\phi_{3}/\varepsilon} - A_{2} (\phi_{2}')^{2} e^{\phi_{2}/\varepsilon} + A_{1} (\phi_{1}')^{2} e^{\phi_{1}/\varepsilon} \right) + \cdots$$

$$= \frac{1}{\varepsilon^{2}} \left( -A_{2} \phi_{2}' (\phi_{2}' - \phi_{3}') e^{\phi_{2}/\varepsilon} + A_{1} \phi_{1}' (\phi_{1}' - \phi_{3}') e^{\phi_{1}/\varepsilon} \right) + \cdots$$
(33)

From the above expression, we observe that v'' = 0 when the exponential terms in equation (33) are of comparable magnitude, requiring the following condition:

$$\operatorname{Re}(\phi_2 + \varepsilon \log(A_2 \phi_2'(\phi_2' - \phi_3'))) = \operatorname{Re}(\phi_1 + \varepsilon \log(A_1 \phi_1'(\phi_1' - \phi_3'))), \tag{34}$$

so that the anti-Stokes line from  $y_C$  must pass through the boundary  $y = \varepsilon L$  (to leading order–equation (34) includes an  $O(\varepsilon)$  perturbation).

Setting (33) to zero produces complex eigenvalues with negative imaginary part and real part around G. If we instead require that the anti-Stokes line from  $y_A$  passes through  $\varepsilon L$ , then we produce the complex conjugate of these eigenvalues, characterised by a positive imaginary part and real part around G.

Note that the calculation above does not consider any potential alterations in the coefficients of the WKB solutions as we pass through the inner region near y = 0. Nevertheless, since the key to determining the eigenvalue lies in understanding the behaviour on the right side of the turning points, which lie in the right half-plane, and in the vicinity of the right-hand boundary, any adjustments in these coefficients do not impact the determination of the eigenvalue. This conclusion is evident from the representation presented in figure 10, where we illustrate the asymptotic and numerical approximation to one eigenfunction. The asymptotic calculation

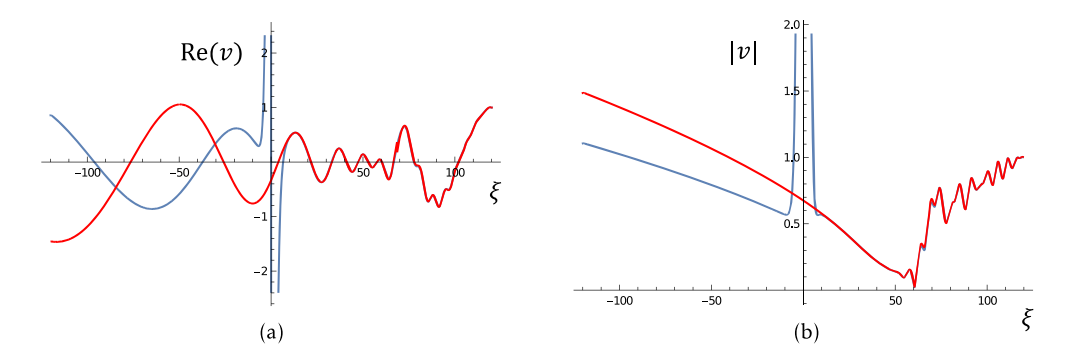


**Figure 10.** The (a) real part and (b) absolute value of the eigenfunction with eigenvalue  $\lambda \approx -0.0243 - 0.1294$ i and G = -0.022, L = 120. The numerical solution is shown in blue, the asymptotic approximation in red. The asymptotic approximation does not take into account the change in amplitude and phase of the WKB approximations across the inner region near the origin, but this does not affect the eigenvalue or the approximation of the eigenfunction in y > 0.

predicts the eigenfunction well for y > 0, but does not take into account the jump in the coefficients of the WKB solution as we pass through the inner region near y = 0; nevertheless this does not affect the eigenvalue calculation.

There is one final scenario that we need to consider, namely when the anti-Stokes line originating from  $y_B$  intersects the right-hand boundary  $y = \varepsilon L$ . This occurs when the eigenvalue,  $\lambda$ , is real, with the corresponding Stokes line configuration illustrated in figure 11. In this configuration, the phases  $\phi_3$  and  $\phi_2$  are approximately of the same magnitude along the real axis, leading to the expression:

$$v = A_3 e^{\phi_3/\varepsilon} - A_2 e^{\phi_2/\varepsilon} + aA_1 e^{\phi_1/\varepsilon}. \tag{35}$$

Similar to the previous analysis, we derive the following leading-order expressions for the derivative of w with respect to y:

$$v' = \frac{1}{\varepsilon} \left( \phi_3' A_3 e^{\phi_3/\varepsilon} - A_2 \phi_2' e^{\phi_2/\varepsilon} + a A_1 \phi_1' e^{\phi_1/\varepsilon} \right) + \cdots, \tag{36a}$$

$$v'' = \frac{1}{\varepsilon^2} \left( (\phi_3')^2 A_3 e^{\phi_3/\varepsilon} - A_2 (\phi_2')^2 e^{\phi_2/\varepsilon} + a A_1 (\phi_1')^2 e^{\phi_1/\varepsilon} \right) + \cdots . \tag{36b}$$

Imposing (14a) at  $y = \varepsilon L$  we determine the coefficient a to leading-order as

$$a = -\frac{A_3 \phi_3' e^{\phi_3/\varepsilon} - A_2 \phi_2' e^{\phi_2/\varepsilon}}{\phi_1' A_1 e^{\phi_1/\varepsilon}}.$$
(37)

This way, equation (36b) simplifies to:

$$v'' = \frac{1}{\varepsilon^{2}} \left( A_{3} (\phi_{3}')^{2} e^{\phi_{3}/\varepsilon} - A_{2} (\phi_{2}')^{2} e^{\phi_{2}/\varepsilon} - \frac{A_{3} \phi_{3}' e^{\phi_{3}/\varepsilon} - A_{2} \phi_{2}' e^{\phi_{2}/\varepsilon}}{\phi_{1}' A_{1} e^{\phi_{1}/\varepsilon}} (\phi_{1}')^{2} A_{1} e^{\phi_{1}/\varepsilon} \right) + \cdots$$

$$= \frac{1}{\varepsilon^{2}} \left( A_{3} \phi_{3}' (\phi_{3}' - \phi_{1}') e^{\phi_{3}/\varepsilon} - A_{2} \phi_{2}' (\phi_{2}' - \phi_{1}') e^{\phi_{2}/\varepsilon} \right) + \cdots$$
(38)

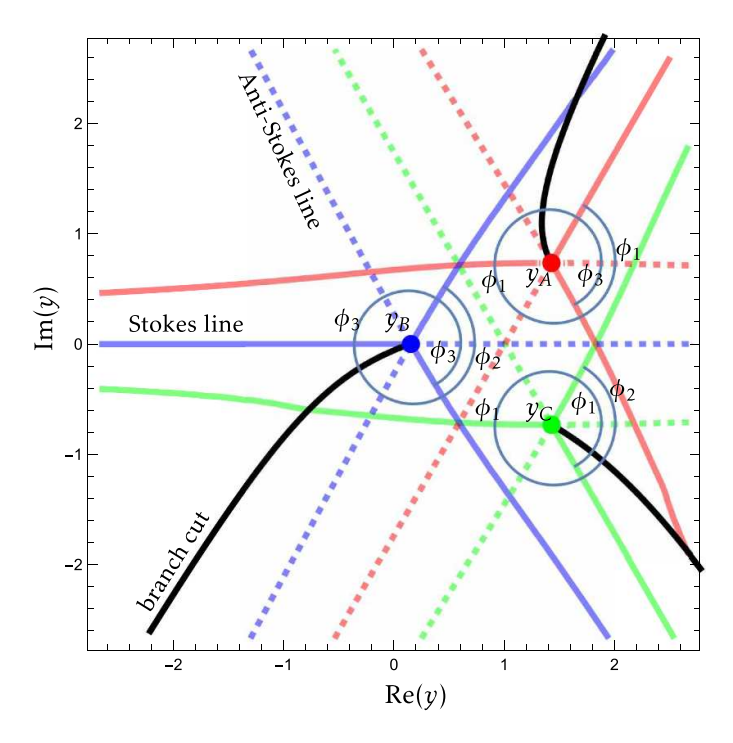


**Figure 11.** Stokes lines (solid) and anti-Stokes lines (dashed) when  $\lambda \approx -0.3$ . Solid black lines are branch-cuts of the phase function  $\phi$ . Three turning points  $y_A$ ,  $y_B$  and  $y_C$  are indicated. Each is a square root branch point of  $\phi$ . The local Riemann surface structure in the vicinity of each branch point is indicated by the spirals, which shows which branches of  $\phi$  are turned on/off across the Stokes lines.

As previously, in order for this expression to be zero, the two exponentials must be of comparable size. Specifically, we derive:

$$Re(\phi_3 + \varepsilon \log(A_3 \phi_3'(\phi_3' - \phi_1'))) = Re(\phi_2 + \varepsilon \log(A_2 \phi_2'(\phi_2' - \phi_1'))).$$
 (39)

When  $\lambda$  is real, for real  $y, \phi_1'$  and  $y_B$  are real, and  $\phi_2 = \bar{\phi}_3$  (with the overbar standing for complex conjugation). Consequently,  $w''(\varepsilon L) = 0$  if

$$e^{2i\text{Im}(\phi_3)/\varepsilon} = \frac{\bar{\phi}_3' \left(\bar{\phi}_3' - \phi_1'\right)}{\left(3 \left(\bar{\phi}_3'\right)^2 - 1 + \varepsilon L\right)^{1/2}} \frac{\left(3 \left(\phi_3'\right)^2 - 1 + \varepsilon L\right)^{1/2}}{\phi_3' \left(\phi_3' - \phi_1'\right)} = e^{i\Phi},$$

say, i.e.

$$\operatorname{Im}(\phi_3) = \varepsilon \left( n\pi + \frac{\Phi}{2} \right). \tag{40}$$

An illustrative example is presented in figure 12, which compares the numerically obtained eigenfunction with the asymptotic approximation for a real eigenvalue  $\lambda \approx -0.0434$ .

In figure 13 we show a comparison of the asymptotic predictions for the eigenvalues along with the numerically-determined spectrum for p = 5.1 and a domain of length L = 120. We see that there is excellent agreement for the complex eigenvalues in branches (A) and (C), and

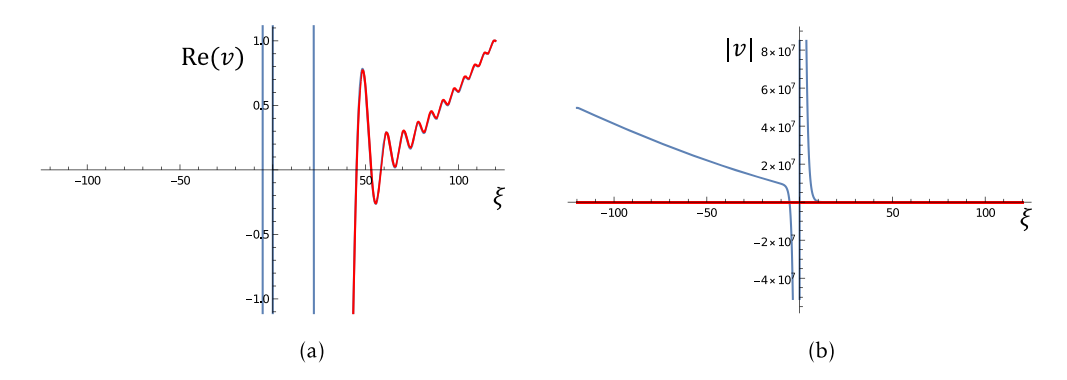


**Figure 12.** The (a) real part and (b) absolute value of the eigenfunction with eigenvalue  $\lambda \approx -0.0434$  for G = -0.022, L = 120. The numerical solution is shown in blue, and the asymptotic approximation in red. Again the approximation does not take into account a jump in the coefficient of the WKB solution near the origin, but this does not affect the eigenfunction for positive y.

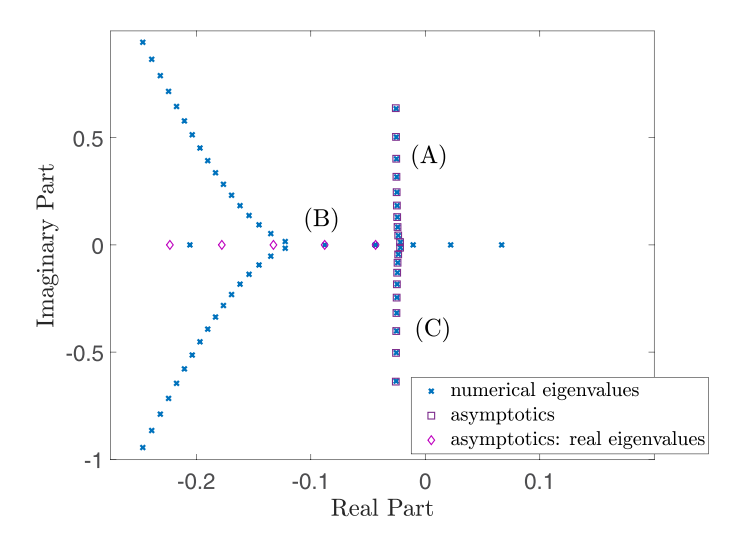


**Figure 13.** Comparison between asymptotic approximation (rectangles and diamonds) and numerical eigenvalues (blue crosses) for domain length, L=120, and parameter, p=5.1 ( $G\approx-0.022$ ). Labels (A), (B) and (C) correspond to the different branches of the asymptotic approximation.

for the first few real eigenvalues in branch (B). However, moving to the left the numerically determined eigenvalues do not stay on the real line, but diverge into a wedge in the complex plane. We believe that this is numerical error, and is caused by the extreme ill-conditioning of the eigenvalue problem. The origin of this can be seen in figure 12—these eigenfunctions are exponentially small near the right-hand boundary by comparison to the left-hand boundary (a factor of  $10^7$  in figure 12 where  $\lambda = -0.0434$  and G = -0.022), and yet the eigenvalue condition is determined by the behaviour at the right-hand boundary.

The previous calculation of real eigenvalues disregards Stokes switching due to the turning points at  $y_A$  and  $y_C$ , which remain exponentially subdominant until  $\lambda$  reaches the region in the complex plane where the first two branches of eigenvalues (A) and (C) intersect the real axis,

i.e. around  $\lambda \approx G$ . Thus the approximations we have found are good at describing each branch of eigenvalues away from the point of intersection of the branches. To get a good approximation near the intersection point we need to incorporate the effects of all the Stokes lines. Doing so we arrive at the following expression

$$v = A_{3}e^{\phi_{3}/\varepsilon} - A_{2}e^{\phi_{2}/\varepsilon} + a\left(A_{1}e^{\phi_{1}/\varepsilon} - A_{3}e^{(\phi_{1}(y_{A}) - \phi_{3}(y_{A}))/\varepsilon}e^{\phi_{3}/\varepsilon} - A_{2}e^{(\phi_{1}(y_{C}) - \phi_{2}(y_{C}))/\varepsilon}e^{\phi_{2}/\varepsilon}\right)$$

$$= \left(1 - ae^{(\phi_{1}(y_{A}) - \phi_{3}(y_{A}))/\varepsilon}\right)A_{3}e^{\phi_{3}/\varepsilon} - \left(1 + ae^{(\phi_{1}(y_{C}) - \phi_{2}(y_{C}))/\varepsilon}\right)A_{2}e^{\phi_{2}/\varepsilon} + aA_{1}e^{\phi_{1}/\varepsilon}. \tag{41}$$

Differentiating equation (41) with respect to y, and considering the leading order, we obtain:

$$v' = \frac{1}{\varepsilon} \left( \left( 1 - a e^{(\phi_{1}(y_{A}) - \phi_{3}(y_{A}))/\varepsilon} \right) \phi_{3}' A_{3} e^{\phi_{3}/\varepsilon} - \left( 1 + a e^{(\phi_{1}(y_{C}) - \phi_{2}(y_{C}))/\varepsilon} \right) A_{2} \phi_{2}' e^{\phi_{2}/\varepsilon}$$

$$+ a A_{1} \phi_{1}' e^{\phi_{1}/\varepsilon} + \cdots,$$

$$(42a)$$

$$v'' = \frac{1}{\varepsilon^{2}} \left( (1 - a e^{(\phi_{1}(y_{A}) - \phi_{3}(y_{A}))/\varepsilon}) (\phi_{3}')^{2} A_{3} e^{\phi_{3}/\varepsilon} - (1 + a e^{(\phi_{1}(y_{C}) - \phi_{2}(y_{C}))/\varepsilon}) A_{2} (\phi_{2}')^{2} e^{\phi_{2}/\varepsilon}$$

$$+ a A_{1} (\phi_{1}')^{2} e^{\phi_{1}/\varepsilon} + \cdots.$$

$$(42b)$$

The value of a in equation (42a) can be determined using (14a) as usual, giving

$$a = -\frac{A_3 \phi_3' e^{\phi_3/\varepsilon} - A_2 \phi_2' e^{\phi_2/\varepsilon}}{\phi_1' A_1 e^{\phi_1/\varepsilon} - e^{(\phi_1(y_A) - \phi_3(y_A))/\varepsilon} \phi_3' A_3 e^{\phi_3/\varepsilon} - e^{(\phi_1(y_C) - \phi_2(y_C))/\varepsilon} A_2 \phi_2' e^{\phi_2/\varepsilon}}.$$
(43)

By substituting equation (43) into equation (42b), we derive:

$$\begin{split} v'' &= -\frac{1}{\varepsilon^2} \frac{A_3 \phi_3' e^{\phi_3/\varepsilon} - A_2 \phi_2' e^{\phi_2/\varepsilon}}{\phi_1' A_1 e^{\phi_1/\varepsilon} - e^{(\phi_1(y_A) - \phi_3(y_A))/\varepsilon} \phi_3' A_3 e^{\phi_3/\varepsilon} - e^{(\phi_1(y_C) - \phi_2(y_C))/\varepsilon} A_2 \phi_2' e^{\phi_2/\varepsilon}} \\ &\times \left\{ \left. (\phi_1')^2 A_1 e^{\phi_1/\varepsilon} - e^{(\phi_1(y_A) - \phi_3(y_A))/\varepsilon} (\phi_3')^2 A_3 e^{\phi_3/\varepsilon} - e^{(\phi_1(y_C) - \phi_2(y_C))/\varepsilon} A_2 (\phi_2')^2 e^{\phi_2/\varepsilon} \right. \right\} \\ &+ \frac{1}{\varepsilon^2} \left( A_3 (\phi_3')^2 e^{\phi_3/\varepsilon} - A_2 (\phi_2')^2 e^{\phi_2/\varepsilon} \right) + \cdots. \end{split}$$

Consequently, after rearranging terms, the eigenvalue condition can be expressed as

$$\frac{A_{3} (\phi_{3}')^{2} e^{\phi_{3}/\varepsilon} - A_{2} (\phi_{2}')^{2} e^{\phi_{2}/\varepsilon}}{A_{3} \phi_{3}' e^{\phi_{3}/\varepsilon} - A_{2} \phi_{2}' e^{\phi_{2}/\varepsilon}} \\
= \frac{(\phi_{1}')^{2} A_{1} e^{\phi_{1}/\varepsilon} - e^{(\phi_{1}(y_{A}) - \phi_{3}(y_{A}))/\varepsilon} (\phi_{3}')^{2} A_{3} e^{\phi_{3}/\varepsilon} - e^{(\phi_{1}(y_{C}) - \phi_{2}(y_{C}))/\varepsilon} A_{2} (\phi_{2}')^{2} e^{\phi_{2}/\varepsilon}}{\phi_{1}' A_{1} e^{\phi_{1}/\varepsilon} - e^{(\phi_{1}(y_{A}) - \phi_{3}(y_{A}))/\varepsilon} \phi_{3}' A_{3} e^{\phi_{3}/\varepsilon} - e^{(\phi_{1}(y_{C}) - \phi_{2}(y_{C}))/\varepsilon} A_{2} \phi_{2}' e^{\phi_{2}/\varepsilon}}.$$
(44)

In figure 14, we illustrate the accuracy of (44) in predicting the complicated behaviour of the negative real eigenvalues associated with the spectrum of self-similar solutions to the gKdV equation as G is varied. The red dots in the plot correspond to the eigenvalues obtained through numerical computation, as visualised previously in figure 7. The solid gray line, on the other hand, represents the asymptotic approximation provided by equation (44). The asymptotic

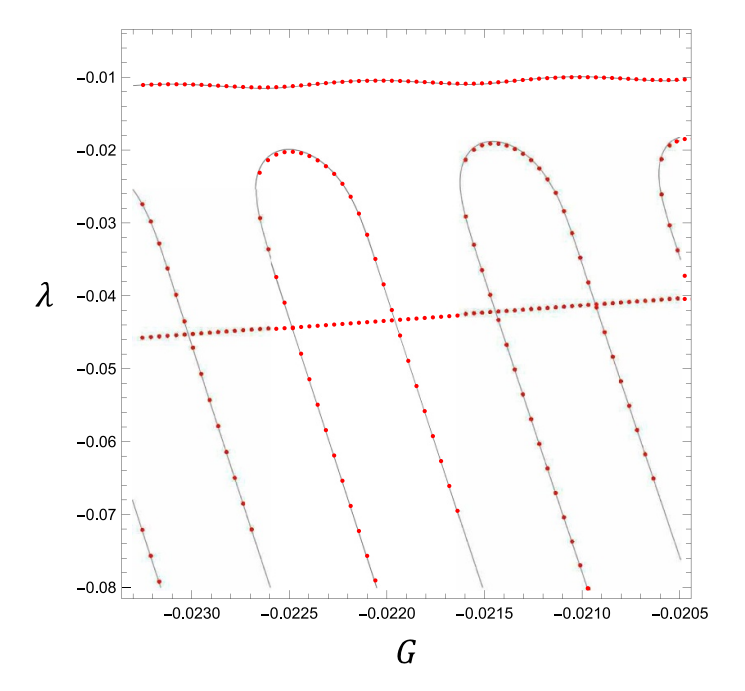


**Figure 14.** Negative real eigenvalues of the operator  $\mathcal{L}$  given by equation (18), branch (B), near the intersection with branches (A) and (C). The real eigenvalues as a function of G are shown with red dots and solid grey line corresponding to the numerical solution of the eigenvalue problem (cf equation (17)) and asymptotic approximation of equation (44), respectively. Note that although the formula captures the slight oscillation of the eigenvalue located near G/2, there is a discrete eigenvalue near 2G which is missing.

formula accurately captures the vast majority of negative eigenvalues, with the exception of a discrete eigenvalue located at 2G.

Ignoring for the moment the eigenvalue near  $\lambda \approx G/2$ , as G is reduced all other negative eigenvalues move towards the origin. The leading eigenvalue is then 'reflected' near  $\lambda \approx G$  and returns to collide with its neighbour (at which point they become complex and add to the eigenvalue branches (A) and (C)).

This eigenvalue dance induces a subtle oscillatory behaviour in the eigenvalue near G/2 (that was also illustrated in the right panel of figure 7, indicated by the solid line and blue open circles), which is also captured well by equation (44).

Finally we note that the leading-order outer equation (cf equation (23)) and BCs are satisfied by  $v \equiv 1$  when  $\lambda = -\varepsilon/2$ , which explains why there is an eigenvalue near  $\lambda \approx G/2$ . However, the eigenfunction predicted by equation (41) is not quite constant in y > 0, as illustrated by the solid red line in figure 15; the approximation effectively captures the small oscillations present in the eigenfunction to the right of the turning point at  $y_B$ .

# 3.4. The normal form

After delving into the spectrum of self-similar solutions in section 3.3, our focus now shifts towards the derivation of the normal form, a pivotal model equation characterizing the emergent bifurcation of the self-similar branch from the soliton branch at p = 5. The final

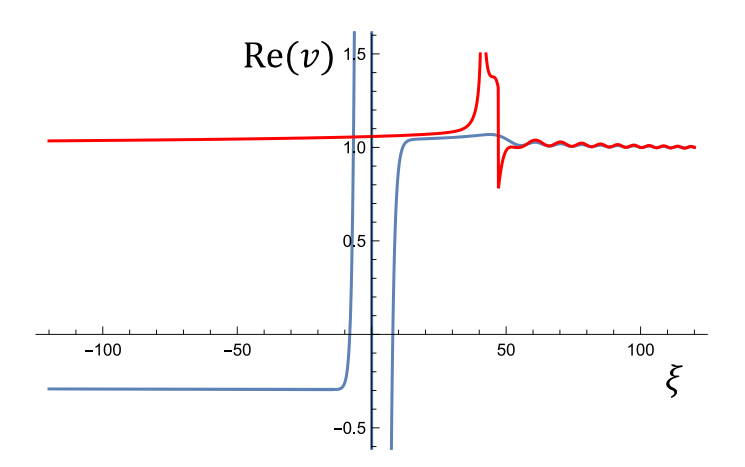


**Figure 15.** The numerically obtained and asymptotically constructed (from equation (41)) eigenfunction with eigenvalue  $\lambda \approx G/2$  is shown with a solid blue and red lines, respectively. The outer solution breaks down near the turning point at  $y_B$ , but captures well the oscillations to the right of this.

expression of this normal form is provided in equation (65) for convenient reference. In the previous section we defined  $\varepsilon = -G$ , expanding  $p = p_0 + \varepsilon p_1 + \cdots$ . In this section we find it convenient to set  $p = p_0 + \varepsilon p_1$ , and expand G in powers of  $\varepsilon$ . We could of course set  $p_1 = 1$ , but since we would like to maintain  $\varepsilon > 0$  while considering both  $p > p_0$  and  $p < p_0$  we find it more convenient to leave  $p_1$  arbitrary. This approach also helps us clearly identify the origin of the terms within the expansion.

We transition to a slower time scale by introducing the transformation  $t = \varepsilon \tau$ . Then equation (12) takes the form

$$\varepsilon \frac{\partial w}{\partial t} = -\frac{\partial^3 w}{\partial \xi^3} - \frac{\partial w^p}{\partial \xi} + G\left(\frac{2}{p-1}w + \xi \frac{\partial w}{\partial \xi}\right) + \frac{\partial w}{\partial \xi},\tag{45}$$

and we note that the blow-up rate, G, continues to be uniquely determined by the pinning condition described in equation (15). Much of the analysis in this section mirrors that in [16] for the steady problem. We expand the solution w and the (constant) blow-up rate G in powers of  $\varepsilon$  as

$$w = \sum_{n=0}^{\infty} \varepsilon^n w_n, \qquad G = \sum_{n=1}^{\infty} \varepsilon^n G_n. \tag{46}$$

Substituting equation (46) into equation (45), we obtain at order  $\mathcal{O}(1)$ :

$$\frac{d^3 w_0}{d\xi^3} + \frac{d}{d\xi} (w_0^{p_0}) - \frac{dw_0}{d\xi} = 0.$$
 (47)

This equation is just that describing steady travelling waves to equation (1), with solution (cf equation (4))

$$w_0 = \left(\frac{p_0 + 1}{2}\right)^{\frac{1}{p_0 - 1}} \operatorname{sech}^{\frac{2}{p_0 - 1}} \left(\frac{(p_0 - 1)}{2} \left(\xi - \xi_0\right)\right). \tag{48}$$

Note that the offset  $\xi_0$  in equation (48) is determined by the pinning condition specified in equation (15), which in this case results in  $\xi_0 = 0$ .

At order  $\mathcal{O}(\varepsilon)$ , considering that  $\partial w_0/\partial t = 0$  and integrating once with respect to  $\xi$ , we find:

$$\mathcal{L}^{(1)}w_1 = -p_1 w_0^{p_0} \log w_0 + G_1 \int_0^{\xi} \left( \frac{2}{p_0 - 1} w_0 + s \frac{\partial w_0}{\partial s} \right) ds + c$$

$$= -p_1 w_0^{p_0} \log w_0 + G_1 g + c, \tag{49}$$

where

$$\mathcal{L}^{(1)}(\cdot) := \frac{\partial^2}{\partial \xi^2} + p_0 w_0^{p_0 - 1} - 1, \quad g = \int_0^{\xi} \left( \frac{2}{p_0 - 1} w_0 + s \frac{\partial w_0}{\partial s} \right) ds, \tag{50}$$

and c is an arbitrary constant of integration. Note that since  $w_0$  (cf equation (48)) is an even function, g (cf equation (50)) is odd. Additionally, we note that since  $\partial w_0/\partial \xi$  satisfies the homogeneous version of equation (49), a solvability condition arises due to the Fredholm alternative. This condition is expressed as follows:

$$0 = G_{1} \int_{-\infty}^{\infty} \frac{\partial w_{0}}{\partial \xi} \int_{0}^{\xi} \left( \frac{2}{p_{0} - 1} w_{0} + s \frac{\partial w_{0}}{\partial s} \right) ds d\xi$$

$$= -G_{1} \int_{-\infty}^{\infty} w_{0} \left( \frac{2}{p_{0} - 1} w_{0} + \xi \frac{\partial w_{0}}{\partial \xi} \right) d\xi$$

$$= -G_{1} \int_{-\infty}^{\infty} \left( \frac{2}{p_{0} - 1} w_{0}^{2} - \frac{w_{0}^{2}}{2} \right) d\xi = \frac{G_{1} (p_{0} - 5)}{2 (p_{0} - 1)} \int_{-\infty}^{\infty} w_{0}^{2} d\xi, \tag{51}$$

due to the relations

$$\int_{-\infty}^{\infty} \frac{\partial w_0}{\partial \xi} w_0^{p_0} \log w_0 \, \mathrm{d}\xi = 0, \qquad \int_{-\infty}^{\infty} \frac{\partial w_0}{\partial \xi} \, \mathrm{d}\xi = 0.$$

From equation (51), it follows that  $p_0 = 5$  when  $G_1 \neq 0$  [45]. Furthermore, the complementary functions can be expressed as:

$$v_1 = \frac{\sinh(2\xi)}{\cosh^{3/2}(2\xi)}, \qquad v_2 = \frac{\cosh(4\xi) - 3}{\cosh^{3/2}(2\xi)},$$

and they satisfy

$$v_1(0) = 0$$
,  $v_2'(0) = 0$ ,  $v_1 \to 0$ ,  $v_2 \to \infty$  as  $|\xi| \to \infty$ 

while also having a Wronskian

$$W = v_1 v_2' - v_2 v_1' = 4.$$

As a result, we can express  $w_1$  as:

$$w_1 = v_1 \int_0^{\xi} \frac{v_2}{4} \left( p_1 w_0^{p_0} \log w_0 - G_1 g - c \right) ds + v_2 \int_{\xi}^{\infty} \frac{v_1}{4} \left( p_1 w_0^{p_0} \log w_0 - G_1 g - c \right) ds.$$
 (52)

With reference to [46]

$$w_1 \sim -c - G_1 g(\infty) = -c + \frac{G_1}{2} \int_0^\infty w_0(\xi) d\xi = -c + \frac{3^{1/4} \Gamma(1/4)^2 G_1}{8\sqrt{2\pi}} \quad \text{as } \xi \to \infty,$$
(53a)

$$w_1 \sim -c - G_1 g(-\infty) = -c - \frac{3^{1/4} \Gamma(1/4)^2 G_1}{8\sqrt{2\pi}} \quad \text{as } \xi \to -\infty.$$
 (53b)

To determine the constant, c, we delve into a more detailed analysis of the far-field region, as discussed in section 3.4.1. First, though, we proceed to one more order in this inner expansion. At order  $\mathcal{O}(\varepsilon^2)$ , upon integrating once with respect to  $\xi$  and rearranging, the result is:

$$\begin{split} \mathcal{L}^{(1)}w_2 &= -\int_{-\infty}^{\xi} \frac{\partial w_1}{\partial t} \, \mathrm{d}s - 10 w_0^3 w_1^2 - p_1 w_0^4 w_1 - 5 p_1 w_0^4 w_1 \log w_0 - \frac{p_1^2}{2} w_0^5 \log^2 w_0 \\ &+ G_1 \int_{-\infty}^{\xi} \left( \frac{w_1}{2} + s \frac{\partial w_1}{\partial s} - \frac{p_1}{8} w_0 \right) \, \mathrm{d}s + c_1 + G_2 \int_0^{\xi} \left( \frac{w_0}{2} + s \frac{\partial w_0}{\partial s} \right) \, \mathrm{d}s, \end{split}$$

where  $c_1$  is an arbitrary constant of integration,

In this case, the solvability condition is given by

$$0 = \int_{-\infty}^{\infty} \frac{\partial w_0}{\partial \xi} \left( -\int_{-\infty}^{\xi} \frac{\partial w_1}{\partial t} ds - 10w_0^3 w_1^2 - p_1 w_0^4 w_1 - 5p_1 w_0^4 w_1 \log w_0 \right)$$

$$- \frac{p_1^2}{2} w_0^5 \log^2 w_0 + G_1 \int_{-\infty}^{\xi} \left( \frac{w_1}{2} + s \frac{\partial w_1}{\partial s} - \frac{p_1}{8} w_0 \right) ds d\xi$$

$$= \int_{-\infty}^{\infty} \frac{\partial w_0}{\partial \xi} \left( -10w_0^3 w_1^2 - p_1 w_0^4 w_1 - 5p_1 w_0^4 w_1 \log w_0 \right) d\xi$$

$$+ G_1 \int_{-\infty}^{\infty} w_0 \left( \frac{w_1}{2} + \frac{p_1}{8} w_0 \right) d\xi + w_0 \frac{\partial w_1}{\partial t} + G_1 \int_{-\infty}^{\infty} \xi \frac{\partial w_0}{\partial \xi} w_1 d\xi.$$

Note that there is a  $p_1$  term in  $w_1$ , so this equation is actually quadratic in  $p_1$ . We can explicitly express the dependence of  $w_1$  on  $p_1$ ,  $G_1$ , and c by writing  $w_1 = p_1 W_1 + G_1 \hat{w}_{\text{odd}} + c \hat{w}_{\text{even}}$  where

$$W_{1} = v_{1} \int_{0}^{\xi} \frac{v_{2}}{4} \left( w_{0}^{5} \log w_{0} \right) ds + v_{2} \int_{\xi}^{\infty} \frac{v_{1}}{4} \left( w_{0}^{5} \log w_{0} \right) ds,$$

$$\hat{w}_{\text{odd}} = -v_{1} \int_{0}^{\xi} \frac{v_{2}g}{4} ds - v_{2} \int_{\xi}^{\infty} \frac{v_{1}g}{4} ds,$$

$$\hat{w}_{\text{even}} = -v_{1} \int_{0}^{\xi} \frac{v_{2}}{4} ds - v_{2} \int_{\xi}^{\infty} \frac{v_{1}}{4} ds.$$

The only time dependence in  $w_1$  arises from  $G_1$  and c. Consequently, the solvability condition simplifies to

$$G_{1} \int_{-\infty}^{\infty} \frac{\partial w_{0}}{\partial \xi} \left( -10w_{0}^{3} 2 \left( p_{1}W_{1} + c\hat{w}_{\text{even}} \right) \hat{w}_{\text{odd}} - p_{1}w_{0}^{4} \left( \hat{w}_{\text{odd}} \right) - 5p_{1}w_{0}^{4} \left( \hat{w}_{\text{odd}} \right) \log w_{0} \right) d\xi$$

$$+ \frac{dc}{dt} \int_{-\infty}^{\infty} w_{0} \hat{w}_{\text{even}} d\xi + G_{1} \int_{-\infty}^{\infty} w_{0} \left( \frac{(p_{1}W_{1} + c\hat{w}_{\text{even}})}{2} + \frac{p_{1}}{8} w_{0} \right) d\xi$$

$$+ G_{1} \int_{-\infty}^{\infty} \xi \frac{\partial w_{0}}{\partial \xi} \left( p_{1}W_{1} + c\hat{w}_{\text{even}} \right) d\xi = 0.$$
(54)

Notably, all quadratic terms in  $p_1$  cancel out (the Authors in [16] get away with omitting these terms). Refining the solvability condition, we arrive at

$$\alpha \frac{\mathrm{d}c}{\mathrm{d}t} = G_1 \left( \beta p_1 + \gamma c \right),\tag{55}$$

where

$$\alpha = -\int_{-\infty}^{\infty} w_0 \hat{w}_{\text{even}} \, \mathrm{d}\xi, \tag{56}$$

$$\beta = \int_{-\infty}^{\infty} \frac{\partial w_0}{\partial \xi} \left( -20w_0^3 W_1 - w_0^4 - 5w_0^4 \log w_0 \right) \hat{w}_{\text{odd}} + w_0 \left( \frac{W_1}{2} + \frac{1}{8} w_0 \right) + \xi \frac{\partial w_0}{\partial \xi} W_1 \, \mathrm{d}\xi, \tag{57}$$

$$\gamma = \int_{-\infty}^{\infty} \left( -20 \frac{\partial w_0}{\partial \xi} w_0^3 \hat{w}_{\text{odd}} + \frac{w_0}{2} + \xi \frac{\partial w_0}{\partial \xi} \right) \hat{w}_{\text{even}} \, \mathrm{d}\xi. \tag{58}$$

Numerically, the coefficients evaluate to:

$$\alpha \approx 0.862705$$
,  $\beta \approx 0.340087$ ,  $\gamma \approx 1.72541$ .

Thus, the steady state [47] of equation (55) becomes

$$p_1 = -c\frac{\gamma}{\beta} \approx -5.07c.$$

It remains to determine c. To do so we need to consider the outer region in which  $\xi$  is large.

3.4.1. Outer region. We now consider the far-field region where  $|\xi| \gg 1$ . In this case,  $w^p$  is negligible since w is exponentially small. Writing  $y = \varepsilon \xi$  as in (21) gives

$$\varepsilon^2 \frac{\partial^3 w}{\partial y^3} - \frac{\partial w}{\partial y} = G_1 \left( \frac{w}{2} + y \frac{\partial w}{\partial y} \right) - \frac{\varepsilon G_1 p_1 w}{8} + \frac{\varepsilon^2 p_1^2 w G_1}{32} - \dots$$
 (59)

As in section 3.3, WKB solutions are sought by using the ansatz

$$w \sim A e^{\phi/\varepsilon}, \quad \varepsilon \downarrow 0,$$
 (60)

and this way, from equation (59), we obtain:

$$(\phi')^3 - \phi' = G_1 y \phi', \tag{61a}$$

$$3A'(\phi')^{2} + 3A\phi'\phi'' - A' = G_{1}\frac{A}{2} + G_{1}yA', \tag{61b}$$

at orders  $\mathcal{O}(\varepsilon^{-1})$  and  $\mathcal{O}(1)$ , respectively. From equation (61a), we find

$$\phi' = \pm (1 + G_1 y)^{1/2}, \tag{62}$$

after which equation (61b) can be integrated to give

$$A = \text{const.} (1 + G_1 y)^{-1/2}. \tag{63}$$

Since  $\phi' = 0$  is also a solution to (61*a*) there is also a non-WKB solution. Setting  $\varepsilon = 0$  in (59) we find that at leading order this solution is

$$w \sim \text{const.} (1 + G_1 y)^{-1/2}$$
.

Putting everything together, we have

$$w \sim \frac{1}{(1+G_1 y)^{1/2}} \left( a_1 + a_2 e^{-\frac{1}{\varepsilon} \int_0^y (1+G_1 s)^{1/2} ds} + a_3 e^{\frac{1}{\varepsilon} \int_0^y (1+G_1 s)^{1/2} ds} \right), \tag{64}$$

for some constants  $a_1$ ,  $a_2$  and  $a_3$ . Note the existence of a turning point at  $y = -1/G_1$ . This will be crucial in the analysis to follow.

We next proceed by separating the cases with  $G_1 < 0$  and  $G_1 > 0$ . We begin first with the case  $G_1 < 0$ .

3.4.2.  $G_1 < 0$ . For y < 0 we need  $a_2 = 0$  in equation (64) otherwise we have exponential growth. So, equation (64) reduces to

$$w \sim \frac{a_1}{(1+G_1y)^{1/2}} + \frac{a_3}{(1+G_1y)^{1/2}} e^{\frac{2}{3G_1\varepsilon} ((1+G_1y)^{3/2}-1)}.$$

Now, in terms of the inner variable, we have:

$$w \sim \frac{a_1}{(1+G_1\varepsilon\xi)^{1/2}} + \frac{a_3}{(1+G_1\varepsilon\xi)^{1/2}} e^{\frac{2}{3G_1\varepsilon}((1+G_1\varepsilon\xi)^{3/2}-1)} \sim a_1 + a_3 e^{\xi} + \cdots,$$

and matching with equation (48), equation (53b) gives

$$a_1 = \left(-c - \frac{3^{1/4}\Gamma(1/4)^2 G_1}{8\sqrt{2\pi}}\right)\varepsilon, \qquad a_3 = 12^{1/4}.$$

On the other hand, and for  $0 < y < -1/G_1$ , we have

$$w \sim \frac{1}{\left(1 + G_1 y\right)^{1/2}} \left( b_1 + b_2 e^{-\frac{2}{3G_1 \varepsilon} \left( (1 + G_1 y)^{3/2} - 1 \right)} + b_3 e^{\frac{2}{3G_1 \varepsilon} \left( (1 + G_1 y)^{3/2} - 1 \right)} \right),$$

for some new constants  $b_i$ . Matching with equation (48), equation (53a) gives  $b_3 = 0$ , as well as

$$b_2 = 12^{1/4}, \qquad b_1 = \left(-c + \frac{3^{1/4}\Gamma(1/4)^2 G_1}{8\sqrt{2\pi}}\right)\varepsilon.$$

For y past the turning point, i.e.  $y > -1/G_1$ , the WKB solution assumes the form

$$w \sim \frac{1}{(-G_1 y - 1)^{1/2}} \left( c_1 + c_2 e^{-\frac{2i}{3G_1 \varepsilon} (-G_1 y - 1)^{3/2}} + c_3 e^{\frac{2i}{3G_1 \varepsilon} (-G_1 y - 1)^{3/2}} \right)$$

for some new constants  $c_i$ . The behaviour at infinity means that  $c_2 = c_3 = 0$ .

Finally, we need to connect the coefficients  $b_i$  with  $c_i$  by matching with a solution in the vicinity of the turning point. Near the turning point, we rescale y in equation (59) according to  $y = -1/G_1 + (2\varepsilon)^{2/3} z/G_1^{1/3}$ , to give, at leading order,

$$\frac{\partial^3 w}{\partial z^3} = 2w + 4z \frac{\partial w}{\partial z},$$

with solution given in terms of Airy functions:

$$w = \alpha_1 \operatorname{Ai}(z)^2 + \alpha_2 \operatorname{Ai}(z) \operatorname{Bi}(z) + \alpha_3 \operatorname{Bi}(z)^2.$$

Those have the asymptotic behaviours

$$\mathrm{Ai}\left(z\right)^{2} \sim \frac{1}{\pi \, |z|^{1/2}} \sin^{2}\left(2/3|z|^{3/2} + \pi/4\right), \qquad \mathrm{Bi}\left(z\right)^{2} \sim \frac{1}{\pi \, |z|^{1/2}} \cos^{2}\left(2/3|z|^{3/2} + \pi/4\right)$$

as  $z \to -\infty$ , and also

$$\operatorname{Ai}(z)^2 \sim \frac{1}{4\pi z^{1/2}} e^{-4/3z^{3/2}}, \qquad \operatorname{Bi}(z)^2 \sim \frac{1}{\pi z^{1/2}} e^{4/3z^{3/2}},$$

as  $z \to \infty$ . The inner limit of the outer is

$$w = \frac{b_1}{|2G_1|^{1/3} \varepsilon^{1/3} z^{1/2}} + \frac{b_2}{|2G_1|^{1/3} z^{1/2} \varepsilon^{1/3}} e^{2/3G_1 \varepsilon} e^{4/3z^{3/2}} \qquad z > 0,$$

$$w = \frac{c_1}{|2G_1|^{1/3} (-z)^{1/2} \varepsilon^{1/3}} \qquad z < 0.$$

To match as  $z \to -\infty$  requires

$$\alpha_1 = \alpha_3 = \frac{c_1 \pi}{|2G_1|^{1/3} \varepsilon^{1/3}}, \qquad \alpha_2 = 0,$$

whereas, to match as  $z \to \infty$  requires:

$$\alpha_3 = \frac{b_2 \pi}{|2G_1|^{1/3} \varepsilon^{1/3}} e^{2/3G_1 \varepsilon}, \qquad b_1 = 0.$$

Thus we finally see that

$$c = \frac{3^{1/4} \Gamma \left(1/4\right)^2 G_1}{8\sqrt{2\pi}}$$

along with

$$\alpha_3 = \alpha_1 = \frac{12^{1/4}\pi}{|2G_1|^{1/3}\varepsilon^{1/3}} e^{2/3G_1\varepsilon}, \qquad c_1 = 12^{1/4} e^{2/3G_1\varepsilon}.$$

Note that there is an exponentially decaying solution reflected back from the turning point, as there was in a previous work on the NLS equation [35], but that the corresponding contribution to the normal form is an exponentially small correction to an algebraic series this time, rather than being the dominant term.

In summary, for  $|y| \to \infty$  and G < 0, we have:

$$\begin{split} w &\sim 12^{1/4} \mathrm{e}^{-2/3|G_1|\varepsilon} \frac{1}{\left(|G_1|y-1\right)^{1/2}} \\ &= 12^{1/4} \mathrm{e}^{-2/3|G|} \frac{1}{\left(|G|\xi-1\right)^{1/2}} \sim \frac{12^{1/4} \mathrm{e}^{-2/3|G|}}{|G|^{1/2} \xi^{1/2}} \text{ as } \xi \to \infty, \\ w &\sim \frac{3^{1/4} \Gamma\left(1/4\right)^2 |G_1|\varepsilon}{4\sqrt{2\pi}} \frac{1}{\left(1-|G_1|y\right)^{1/2}} \\ &= \frac{3^{1/4} \Gamma\left(1/4\right)^2 |G|}{4\sqrt{2\pi}} \frac{1}{\left(1-|G|\xi\right)^{1/2}} \sim \frac{3^{1/4} \Gamma\left(1/4\right)^2}{4\sqrt{2\pi}} \frac{|G|^{1/2}}{\left(-\xi\right)^{1/2}} \text{ as } \xi \to \infty, \end{split}$$

which agrees with [16] after correcting the missing factor of 2 in their expression for C.

3.4.3.  $G_1 > 0$ . For y > 0 we need  $a_3 = 0$  in equation (64) otherwise we have exponential growth. This way, we have:

$$w \sim \frac{a_1}{(1+G_1y)^{1/2}} + \frac{a_2}{(1+G_1y)^{1/2}} e^{-\frac{2}{3G_1\varepsilon}((1+G_1y)^{3/2}-1)},$$

and in terms of the inner variable

$$w \sim \frac{a_1}{(1+G_1\varepsilon\xi)^{1/2}} + \frac{a_2}{(1+G_1\varepsilon\xi)^{1/2}} e^{-\frac{2}{3G_1\varepsilon}((1+G_1\varepsilon\xi)^{3/2}-1)} \sim a_1 + a_2 e^{-\xi} + \cdots$$

Matching now with equation (48), equation (53a) gives

$$a_1 = \left(-c + \frac{3^{1/4}\Gamma(1/4)^2 G_1}{8\sqrt{2\pi}}\right)\varepsilon,$$
  

$$a_2 = 12^{1/4}.$$

For  $-1/G_1 < y < 0$  we have

$$w = \frac{1}{(1+G_1y)^{1/2}} \left( b_1 + b_2 e^{-\frac{2}{3G_1\varepsilon} \left( (1+G_1y)^{3/2} - 1 \right)} + b_3 e^{\frac{2}{3G_1\varepsilon} \left( (1+G_1y)^{3/2} - 1 \right)} \right),$$

while for  $y < -1/G_1$  we have

$$w = \frac{1}{(-G_1 y - 1)^{1/2}} \left( c_1 + c_2 e^{-\frac{2i}{3G_1 \varepsilon} (-G_1 y - 1)^{3/2}} + c_3 e^{\frac{2i}{3G_1 \varepsilon} (-G_1 y - 1)^{3/2}} \right).$$

The behaviour at infinity means that  $c_2 = c_3 = 0$ . Again, matching with equation (48), equation (53b) gives  $b_2 = 0$ , and

$$b_3 = 12^{1/4}, \qquad b_1 = \left(-c - \frac{3^{1/4}\Gamma(1/4)^2 G_1}{8\sqrt{2\pi}}\right)\varepsilon.$$

This time, the inner limit of the outer near the turning point is

$$w = \frac{b_1}{(2G_1)^{1/3} \varepsilon^{1/3} z^{1/2}} + \frac{b_3}{(2G_1)^{1/3} z^{1/2} \varepsilon^{1/3}} e^{-2/3G_1 \varepsilon} e^{4/3z^{3/2}} \qquad z > 0,$$

$$w = \frac{c_1}{(2G_1)^{1/3} (-z)^{1/2} \varepsilon^{1/3}} \qquad z < 0.$$

To match as  $z \to -\infty$  requires

$$\alpha_1 = \alpha_3 = \frac{c_1 \pi}{(2G_1)^{1/3} \varepsilon^{1/3}}, \qquad \alpha_2 = 0,$$

whereas as  $z \to \infty$  requires

$$\alpha_3 = \frac{b_3 \pi}{(2G_1)^{1/3} \varepsilon^{1/3}} e^{-2/3G_1 \varepsilon}, \qquad b_1 = 0.$$

Thus we finally see that

$$c = -\frac{3^{1/4}\Gamma(1/4)^2 G_1}{8\sqrt{2\pi}},$$

along with

$$\alpha_3 = \alpha_1 = \frac{12^{1/4}\pi}{(2G_1)^{1/3}\varepsilon^{1/3}} e^{-2/3G_1\varepsilon}, \qquad c_1 = 12^{1/4} e^{-2/3G_1\varepsilon}.$$

3.4.4. Comparison of normal form against numerics. Combining the results for  $G_1$  positive and negative, we finally have

$$c = -C|G_1|, \qquad C = \frac{3^{1/4}\Gamma(1/4)^2}{8\sqrt{2\pi}}.$$

Thus the normal form (cf equation (55)) becomes

$$\alpha C \frac{\mathrm{d}G_1}{\mathrm{d}t} = -|G_1|\beta p_1 + \gamma C G_1^2. \tag{65}$$

In figure 16, we provide a comparative analysis of the blow-up rate computed using the self-similar dynamics (cf equation (12)) (represented by the dashed-dotted black line) and the normal form (indicated by red dots). The left panel shows the case for p = 5.01, which is in close proximity to the bifurcation point. Conversely, the right panel illustrates the case for p = 5.1. In the left panel, one can observe a very good agreement between the self-similar dynamics and the normal form. However, as we move away from p = 5 (as seen in the right panel), a disparity emerges between the two approaches. (See also the left panel in figure 4 which shows the growing disparity between numerics and normal form as we move away from p = 5.) Notably, both curves still maintain a consistent qualitative trend, indicating a comparable rate of asymptotic convergence towards a self-similar profile.

It is interesting to compare (65) with the modulation equations given by Lan [30]. For G < 0 we may write (65) as

$$\frac{\mathrm{d}G}{\mathrm{d}\tau} \approx \frac{\beta (p-5)}{\alpha C} G + \frac{\gamma}{\alpha} G^2 = \frac{\gamma}{\alpha} G (G - G_c), \tag{66}$$

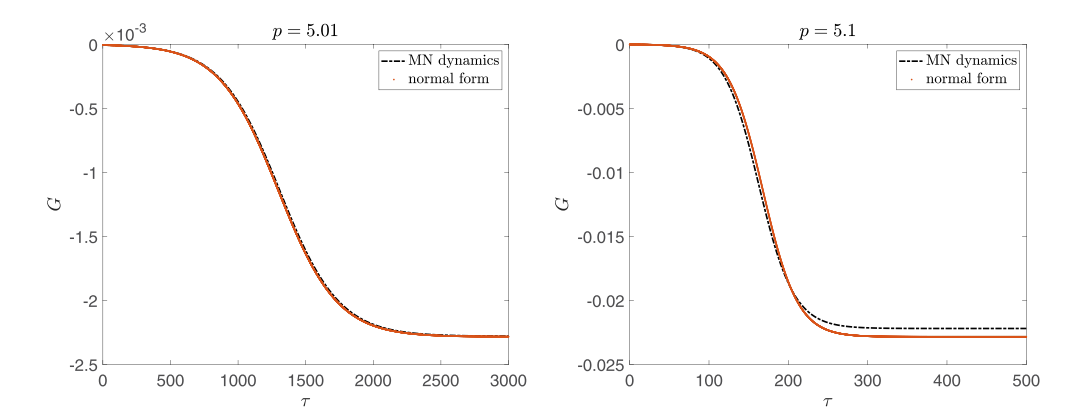


**Figure 16.** The evolution of the blow-up rate G as a function of  $\tau$  computed by the self-similar dynamics of equation (12) and normal form of equation (65) are shown with a dashed-dotted black line and red dots, respectively, for values of p = 5.01 (left panel) and p = 5.1 (right panel).

say, where

$$G_c = -\frac{\beta (p-5)}{\gamma C}$$

is the steady-state solution (corresponding to self-similar blow-up). Lan considers dynamics only close to blow-up, i.e. in the limit in which  $|G - G_c| \ll G_c$ . There are three evolution equations given in [30] (equations (3.6)–(3.8) there), for the width of the collapsing profile, its centre, and an auxilliary parameter b, which is -G in our notation. Translated to our notation, the first of these equations is  $G \approx G_c$ , while the second is our equation (11). The third gives

$$\frac{\mathrm{d}G}{\mathrm{d}\tau}\approx c_p G_c \left(G-G_c\right),\,$$

which is the linearisation of (66) about  $G = G_c$ , if we identify Lan's parameter  $c_p$  with  $\gamma/\alpha$ . Curiously Lan shows  $c_p = 2 + O(|p-5|)$ , which means  $\gamma/\alpha = 2$ , a result which we find to be true numerically, but which is not obvious from the definitions (56) and (58).

#### 4. Conclusions and future challenges

In the present work we have revisited the gKdV equation, by considering the bifurcation of its solitary waves into instability, as the exponent of the generalised nonlinearity crossed the value of p=5. Building on the work of [16, 24], upon exploring the stability of the solitary wave solutions with blow-up rate G=0, we retrieved the self-similar solutions with non-vanishing blow-up rate  $G\neq 0$  which were found both dynamically, as well as statically as stationary states in the so-called co-exploding frame. One of the key contributions of the present work involves the elucidation of the bifurcation associated with the emergence of this self-similar branch of solutions past the critical point of p=5; we found this bifurcation to bear features of a pitchfork (through the presence of two mirror symmetric blow-up solutions), as well as to encompass linear (in absolute value) and quadratic terms in its normal form (a feature somewhat reminiscent of a transcritical normal form). We have discussed both the similarities and

the differences of the relevant phenomenology from that of the other prototypical dispersive nonlinear PDE, namely the NLS which features a similar bifurcation, but an exponentially deviating branch past the corresponding critical point.

The second key contribution of the present work concerns the spectral stability analysis of the emerging self-similar branch. In connection with the latter, we elucidate both the trajectory of the eigenvalues of the point spectrum, such as the ones at -3G (due to the former scaling invariance in the original frame) or at -G (due to the former translational invariance at the original frame), or the one at (nearly) G/2, but also those of the continuous spectrum. The latter consists of two main bands, one of which aligns (as it is better resolved) with the vertical line  $\lambda = G$ , while the other we argued to be extremely ill-conditioned and cannot be resolved. If they could be resolved, these eigenvalues would move to the negative real axis. Instead, what we find is that we can only resolve the first few of them. Moreover, the rest becomes harder to resolve as the domain size L gets larger, leading the corresponding eigenvalue wedge to become more vertical rather than more horizontal. This is rather telling as regards the complexity of the corresponding spectrum and the difficulty to numerically pin it down.

The addressing of the above challenges paves the way for the further consideration of a number of interesting problems in this context of self-similar dynamics. As concerns the case of the gKdV, having addressed the existence and stability of the self-similar states, it would be useful to understand better the fully nonlinear dynamics in both the original (non-exploding) and the presently considered (co-exploding) frame in line with important earlier dynamical observations, such as those of, e.g. [25]. In particular, the dynamical reshaping of the structure (for different initial conditions) into a self-similarly collapsing waveform constitutes an intriguing dynamical question. It is also interesting to extend relevant existence/stability/dynamical considerations beyond conservative cases such as the generalised NLS and KdV, where it seems that the emergent instabilities in the co-exploding frame are only apparent/fictitious ones related to symmetries of the original frame, but not true dynamical instabilities. In that vein, a particularly intriguing example to consider concerns the non-conservative case of the complex Ginzburg-Landau equation earlier considered in the work of [48]. There, there exist both branches that stem from the NLS and ones that do not (in the limit of small dissipation) and both branches that are stable and ones that are unstable in the co-exploding frame. Hence, it will be quite interesting to expand existence/stability, but also importantly dynamics considerations to such states in future works.

# Data availability statement

The data that support the findings of this study are available upon reasonable request from the authors.

# **Acknowledgments**

E G C expresses his gratitude to Professors Uri M Ascher (University of British Columbia), Raymond Spiteri (University of Saskatchewan), Eva Weinmüller (Vienna University of Technology) as well as Linda Petzold (University of California Santa Barbara) for fruitful discussions. This work has been supported by the U.S. National Science Foundation under Grants DMS-2204782 (EGC) and DMS-2110030 and DMS-2204702 (PGK). The work of IGK was partially supported by the US-DoE.

#### **ORCID iDs**

#### References

- [1] Ablowitz M J and Clarkson P A 1991 Solitons, Nonlinear Evolution Equations and Inverse Scattering (Cambridge University Press)
- [2] Whitham G B 1974 Linear and Nonlinear Waves (Wiley)
- [3] Ablowitz M J 2011 Nonlinear Dispersive Waves: Asymptotic Analysis and Solitons (Cambridge University Press)
- [4] Dauxois T and Peyrard M 2006 Physics of Solitons (Cambridge University Press)
- [5] Zabusky N J and Kruskal M D 1965 Interaction of "solitons" in a collisionless plasma and the recurrence of initial states *Phys. Rev. Lett.* 15 240
- [6] Fermi E, Pasta J and Ulam S 1955 Studies of nonlinear problems. I Technical Report LA-1940 (Los Alamos National Laboratory)
- [7] Gallavotti G 2008 The Fermi-Pasta-Ulam Problem: A Status Report (Springer)
- [8] Zabusky N J 1967 A synergetic approach to problems of nonlinear dispersive wave propagation and interaction Nonlinear Partial Differential Equations: A Symposium on Methods of Solution ed W F Ames (Academic)
- [9] Korteweg D J and de Vries G 1895 On the change of form of long waves advancing in a rectangular canal and on a new type of long stationary waves *Phil. Mag.* 5 422–43
- [10] Olver P J 1977 Evolution equations possessing infinitely many symmetries J. Math. Phys. 18 1212-5
- [11] Hirota R 2004 The Direct Method in Soliton Theory (Cambridge University Press)
- [12] Remoissenet M 1999 Waves Called Solitons: Concepts and Experiments (Springer)
- [13] Osborne A R 2010 Nonlinear Ocean Waves And The Inverse Scattering Transform (Academic)
- [14] Nakamura Y and Tsukabayashi I 1985 Modified Korteweg-de Vries ion-acoustic solitons in a plasma J. Plasma Phys. 34 402–15
- [15] Bona J L, Souganidis P E and Strauss W A 1987 Stability and instability of solitary waves of Korteweg-de Vries type Proc. R. Soc. A 411 395–412
- [16] Amodio P, Budd C J, Koch O, Rottschäfer V, Settanni G and Weinmüller E 2020 Near critical, self-similar, blow-up solutions of the generalised Korteweg-de Vries equation: asymptotics and computations *Physica* D 401 132179
- [17] Sulem C and Sulem P L 1999 The Nonlinear Schrödinger Equation (Springer)
- [18] Merle F 2001 Existence of blow-up solutions in the energy space for the critical generalized KdV equation *J. Am. Math. Soc.* **14** 555–78
- [19] Martel Y and Merle F 2002 Stability of blow-up profile and lower bounds for blow-up rate for the critical generalized KdV equation Ann. Math. 155 235–80
- [20] Weinstein M I 1983 Nonlinear Schrödinger equations and sharp interpolation estimates Commun. Math. Phys. 87 567–76
- [21] Pego R L and Weinstein M I 1992 Eigenvalues and instabilities of solitary waves *Phil. Trans. R. Soc.* A 340 47–94
- [22] Bona J L, Dougalis V A, Karakashian O A and McKinney W R 1995 Conservative, high-order numerical schemes for the generalized Korteweg-de Vries equation *Phil. Trans. R. Soc.* A 351 107–64
- [23] Dix D B and McKinney W R 1998 Numerical computations of self-similar blow-up solutions of the generalized Korteweg-de Vries equation *Differ. Integral Equ.* 11 679–723
- [24] Koch H 2015 Self-similar solutions to super-critical gKdV Nonlinearity 28 545–75
- [25] Klein C and Peter R 2015 Numerical study of blow-up and dispersive shocks in solutions to generalized Korteweg-de Vries equations *Physica* D 304–305 52–78
- [26] Klein C 2008 Fourth-order time-stepping for low dispersion Korteweg-de Vries and nonlinear Schrödinger equations Electron. Trans. Numer. Anal. 29 116–35

- [27] Martel Y, Merle F and Raphaël P 2014 Blow-up for the critical generalized Korteweg-de Vries equation. I: Dynamics near the soliton Acta. Math. 212 59–140
- [28] Martel Y, Merle F and Raphaël P 2015 Blow-up for the critical generalized Korteweg-de Vries equation. II: Minimal mass dynamics J. Eur. Math. Soc. 17 1855–925
- [29] Kitzhofer G, Pulverer G, Simon C, Koch O and Weinmüller E 2010 The new MATLAB solver BVPSUITE for the solution of singular implicit BVPs JNAIAM J. Numer. Anal. Ind. Appl. Math. **5** 113–34
- [30] Lan Y 2016 Stable self-similar blow-up dynamics for slightly  $L^2$ -supercritical generalized KDV equations Commun. Math. Phys. 345 223-69
- [31] Siettos C I, Kevrekidis I G and Kevrekidis P G 2003 Focusing revisited: a renormalization/bifurcation approach Nonlinearity 16 497–506
- [32] LeMesurier B J, Papanicolaou G C, Sulem C and Sulem P L 1986 Focusing and multi-focusing solutions of the nonlinear Schrödinger equation Physica D 31 78-10
  - LeMesurier B J, Papanicolaou G C, Sulem C and Sulem P L 1988 Local structure of the selffocusing singularity of the nonlinear Schrödinger equation Physica D 32 210-26
- [33] McLaughlin D W, Papanicolaou G C, Sulem C and Sulem P L 1986 Focusing singularity of the cubic Schrödinger equation Phys. Rev. A 34 1200-10
- [34] Kopell N and Landman M J 1995 Spatial structure of the focusing singularity of the nonlinear Schrödinger equation: a geometrical analysis SIAM J. Appl. Math. 55 1297–323
- [35] Chapman S J, Kavousanakis M, Kevrekidis I G and Kevrekidis P G 2021 Normal form for the onset of collapse: the prototypical example of the nonlinear Schrödinger equation Phys. Rev. E
- [36] Jon Chapman S, Kavousanakis M, Charalampidis E G, Kevrekidis I G and Kevrekidis P G 2022 A spectral analysis of the nonlinear Schrödinger equation in the co-exploding frame *Physica* D **439** 133396
- [37] Bernoff A J and Witelski T P 2010 Stability and dynamics of self-similarity in evolution equations J. Eng. Math. 66 11-31
- [38] Hairer E, Nørsett S P and Wanner G 1993 Solving Ordinary Differential Equations I (Springer)
- [39] Kuznetsov Y A 2023 Elements of Applied Bifurcation Theory 4th edn (Springer)
- [40] Bender C M and Orszag S A 1999 Advanced Mathematical Methods for Scientists and Engineers, Asymptotic Methods and Perturbation Theory (Springer)
- [41] Meyer R E 1989 A simple explanation of the Stokes phenomenon SIAM Rev. 31 435–45
- [42] Paris R B and Wood A D 1995 Stokes phenomenon demystified IMA Bull. 31 21–28
- [43] Olde Daalhuis A B, Chapman S J, King J R, Ockendon J R and Tew R H 1995 Stokes phenomenon and matched asymptotic expansions SIAM J. Appl. Math. 55 1469-83
- [44] Chapman S J 2002 Subcritical transition in channel flows J. Fluid Mech. 451 35-97
- [45] Note that the work of [16] does not include the first term on the RHS of Equation 49. However, omitting this term does not affect the solvability condition. Essentially the analysis in [16] perturbs only the p which appears as a coefficient, not that which appears as an exponent, that is, they solve

$$\frac{\partial w}{\partial \tau} = -\frac{\partial^3 w}{\partial \xi^3} - \frac{\partial w^5}{\partial \xi} + G\left(\frac{2}{p-1}w + \xi \frac{\partial w}{\partial \xi}\right) + \frac{\partial w}{\partial \xi}.$$

- $\frac{\partial w}{\partial \tau} = -\frac{\partial^3 w}{\partial \xi^3} \frac{\partial w^5}{\partial \xi} + G\left(\frac{2}{p-1}w + \xi\frac{\partial w}{\partial \xi}\right) + \frac{\partial w}{\partial \xi}.$  [46] We note that there is a missing factor of 2 in the corresponding equations in [16].
- [47] If we followed [16] and missed out all the terms associated with perturbing the power, then we would find

would find 
$$p_1 = -c \frac{\displaystyle \int_{-\infty}^{\infty} \left( -20 \frac{\partial w_0}{\partial \xi} w_0^3 \hat{w}_{\rm odd} + \frac{w_0}{2} + \xi \frac{\partial w_0}{\partial \xi} \right) \hat{w}_{\rm even} \, \mathrm{d}\xi}{\displaystyle \int_{-\infty}^{\infty} \frac{1}{8} w_0^2 \, \mathrm{d}\xi} \approx -5.07c.$$
 It seems like the extra terms integrate to zero, i.e. 
$$\int_{-\infty}^{\infty} \frac{\partial w_0}{\partial \xi} \left( -20 w_0^3 W_1 - w_0^4 - 5 w_0^4 \log w_0 \right) \hat{w}_{\rm odd} + \left( \frac{w_0}{2} + \xi \frac{\partial w_0}{\partial \xi} \right) W_1 \, \mathrm{d}\xi = 0$$
 though we have been unable to show this.

$$\int_{-\infty}^{\infty} \frac{\partial w_0}{\partial \xi} \left( -20w_0^3 W_1 - w_0^4 - 5w_0^4 \log w_0 \right) \hat{w}_{\text{odd}} + \left( \frac{w_0}{2} + \xi \frac{\partial w_0}{\partial \xi} \right) W_1 \, d\xi = 0$$

[48] Budd C J, Rottschäfer V and Williams J F 2005 Multibump, blow-up, self-similar solutions of the complex Ginzburg-Landau eqaution SIAM J. Appl. Dyn. Sys. 4 649-78